Science

AAAS

Supplementary Materials for

Dense functional and molecular readout of a circuit hub in sensory cortex

Cameron Condylis *et al*.

Corresponding author: Jerry L. Chen, jerry@chen-lab.org

The PDF file includes:

Materials and Methods
Supplementary Text
Figs. S1 to S22
References

Other Supplementary Material for this manuscript includes the following:

Tables S1 and S2
Movie S1
MDAR Reproducibility Checklist

Materials and Methods

Mice. Experiments in this study were approved by the Institutional Animal Care and Use Committee at Boston University, approved by the Allen Institute Animal Care and Use Committee, and conform to NIH guidelines. Behavior experiments were performed using C57BL/6J mice (The Jackson Laboratory). Input mapping experiments were performed using SST-IRES-Cre and VIP-IRES-Cre mice[42]. Bilateral whisker deprivation experiments were performed using B6.CgTg(Fos/EGFP)1-3Brth/J mice[30]. All animals were 6-8 weeks of age at time of surgery. Mice used for behavior were housed individually in reverse 12-hour light cycle conditions. All handling and behavior occurred under simulated night time conditions.

Single cell RNA sequencing analysis. Single cell RNA sequencing data in this study were previously acquired. S1 excitatory and inhibitory subclasses and cell types obtained were identified using an iterative clustering R package hicat (https://github.com/AllenInstitute/hicat) as previously described[1]. To understand the cell type and area differences of L2/3 neurons among S1, V1, and ALM, differentially expressed genes (DEG) were identified between all pairs of cell types, all pairs of areas, and all pairs of cell type and area groups (fold change > 4, FDR 0.01, and expressed in >= 40% cells in one group). The average counts per million reads mapped (CPM) values of each DEG within each group were scaled across all the groups to between 0 and 1. A DEG was categorized as cell type specific if its normalized values were greater than 0.5 in at least two areas (or one region if the cluster is specific to one area) within a given cell type, and area-specific if its scaled values were greater than 0.5 in at least two cell types within a given area. DEGs specific to both cell type and area were defined as genes with scaled value greater than 0.5 in only one area and cell type. Immediate early genes enriched in Baz1a neurons were identified as those with statistically higher CPM values compared to Adamts2 and Agmat neurons.

Animal imaging preparation. For behavior and bilateral whisker deprivation experiments, the genetically encoded calcium indicator RCaMP1.07[20] was expressed by stereotaxic injection of AAV2/PHP.eb-RCaMP1.07 into S1 (600 nL, ~1 × 10^9 vg/ml per virus). L2/3 was targeted at 1.1 mm posterior to bregma, 3.3 mm lateral, 300 μm below the pial surface. A 4mm cranial window was implanted over S1 to obtain optical access[31]. A metal headpost was implanted on the skull adjacent to the window to allow for head fixation. One week after window implantation and injections, animals were handled and acclimated to head fixation. In order to identify regions of S1 that correspond to specific whiskers, functional mapping was performed using intrinsic signal imaging.

Behavioral task. Animals were trained on a head-fixed, whisker-based delayed non-match to sample task using equipment and training protocol previously described[24]. Whiskers were trimmed to a single row corresponding to the selected imaging region for high-speed videography. Animals were water deprived throughout training and imaging and only received water by performing the task. Their weight was monitored daily to ensure body weight did not drop below 80% of initial weight. In the task, a motorized rotor was used to deflect whiskers in either an anterior or posterior direction. During the delay period and inter-trial interval, the rotor was withdrawn to prevent whisker-rotor contact. Behavior was reported as 'go/no-go' in which animals licked on 'go' trials for a water reward ('hit') when the presented sample and test stimulus were non-matching and withheld licking on 'no-go' trials ('correct rejection') when the presented

sample and test stimulus were matching. Misses on go trials were not rewarded, and false alarms on no-go trials were punished with an air puff and a time-out period.

Bilateral whisker deprivation. Awake, head-fixed animals were subjected to passive whisker deflection. Each trial had the following structure: baseline (3s), rotor approach, anterior rotation and whisker deflection (1s), posterior rotation and whisker deflection (1s). The rotor was positioned 1-2mm from the face to provide consistent whisker stimulation before and after bilateral deprivation. For baseline activity and fosGFP measurements, neurons were imaged for two days prior to deprivation (Day -2 and -1). Whiskers were trimmed bilaterally and imaged immediately afterwards (Day 0). The principle whisker was trimmed to a stub ~1-2 mm in length, so that it would not provide sensory information to the animal but could still be deflected by the rotor. Whiskers were re-trimmed every other day. During deprivation, activity measurements were acquired at Day 1 and 5 while fosGFP measurements were acquired at Day 1, 3, and 5.

Two-photon imaging. Two-photon calcium imaging in expert animals was performed with a custom-built resonant-scanning multi-area two-photon microscope with 16x/0.8NA water immersion objective (Nikon) using custom-written Scope software as previously described. A 31.25 MHz 1040 nm fiber laser (Spark Lasers) was used to excite the red calcium indicator RCaMP1.07. The multi-area two-photon microscope was configured to perform simultaneous imaging at 32.6 Hz frame rate of two imaging planes were separated by ~50 μm in depth. Average power of each beam at the sample was 70-90mW. For each animal, imaging was performed across 8-10 behavioral sessions (**Fig. S7**). For bilateral whisker deprivation experiments, calcium imaging was performed across 16 different fields of view (FOV) per animal for each imaging session (**Fig. S17**). Each FOV was acquired for 50 trials. For imaging fosGFP expression, a dual channel high resolution 3D stacks of RCamp1.07 and GFP were taken through the calcium-imaged area using a Ti:Sapphire laser tuned to 860 nm (Chameleon Ultra Laser; Coherent) and resolved using 630/69nm and 520/60nm emission filters (BrightLine), respectively. Following the conclusion of all experiments, animals were anesthetized and a high resolution 3D image volume was taken through the imaged area(s) for later registration with *ex vivo* tissue.

Whisker tracking and analysis. High-speed videography of whisker movement was acquired at 500 Hz as previously described(*24, 52*). For analysis, whiskers were automatically traced(*52*). The angle, curvature (κ), and location of the whisker tip at each time point was extracted for all traced whiskers. Using the mean whisker angle, a Hilbert transform was applied to determine whisking amplitude, phase, setpoint, and the reconstructed whisker angle (angleRECONSTRUCTION)(*53*). The position of the rotor was automatically tracked in the video using custom scripts (MATLAB). Whisker-rotor touch was scored as events in which the tip of at least one whisker came into within <5 pixel radius of the rotor face with 'touch onset' defined as the first possible whisker contact at the beginning of the sample and test period and 'touch offset' defined as the last possible whisker contact at the end of the sample and test period. Time vectors of kinematic parameters were down-sampled to the imaging frame rate for further analysis. Behavioral sessions with sub-optimal imaging conditions in which whisker tracking failed in >20% of trials were excluded from analysis.

In vivo **image analysis.** All image processing was performed in MATLAB as described(*24, 53*). Two-photon images were first motion corrected using a piece-wise rigid motion correction

algorithm(*54*). For behavior experiments, regions of interest (ROIs) were extracted using constrained non-negative matrix factorization and were labeled as active neurons. A global neuropil correction was performed for each active neuron and the resulting fluorescence traces were detrended on a per trial basis. Remaining neurons in the FOV were manually segmented and labeled as inactive neurons. For bilateral whisker deprivation experiments, neurons across imaging sessions were identified by first registering each session image into a global reference image using ImageJ and MATLAB. For each neuron, ROIs were manually segmented in the reference image and applied to each session image for extraction of calcium signals. For analysis of fosGFP expression, 3D volume stacks across imaging sessions were aligned by landmark-based 3D affine registration using custom software (Neurotator). Automatically segmented 3D ROIs were obtained from registered *ex vivo* tissue slices corresponding to *in vivo* imaged areas and were overlaid for each imaged neuron. The mean fluorescence intensity for GFP and RCamp1.07 was extracted for each ROI. To control for variability in imaging conditions and background fluorescence, relative GFP intensity was expressed as $\Delta R/R_0 = (R_{ROI}-R_{neuropil})/R_{neuropil}$ where R_{ROI} is the ratio between GFP and RCaMP1.07 fluorescence in the ROI and $R_{neuropil}$ is the ratio between GFP and RCaMP1.07 fluorescence in the surrounding neuropil. FosGFP neurons with $\Delta R/R_0 > 0.2$ were identified as high expressing.

Calcium event estimation. Calcium signals were deconvolved using an Online Active Set method to Infer Spikes (OASIS), a generalization of the pool adjacent violators algorithm (PAVA) for isotonic regression. First, calcium signals below baseline fluorescence (bottom 10th percentile of signal intensity) were thresholded. For each cell, a convolution kernel with exponential rise and decay time constants were determined using an autoregressive model. For measurement of photon shot noise, signal-to-noise (*v*) was calculated as for each cell:

$$1) \quad v = \frac{Median_t|F_{t+1}-F_t|}{\sqrt{f_r}}$$

where the median absolute difference between two subsequent time points of the fluorescence trace, *F*, is divided by the square root of the frame rate, f_r (*55*). The convolution kernel was applied to the calcium signals to obtain an initial deconvolved signal that was then normalized by the signal-to-noise resulting in a calcium event estimate ($\hat{s}$). These values were thresholded to $\hat{s} = 1$, producing binary events that represent an estimated spiking-related calcium event (see **Text S2**).

Trans-monosynaptic rabies tracing. For input mapping experiments, trans-monosynaptic rabies tracing was performed on transgenic SST-IRES-Cre or VIP-IRES-Cre mice. AAV1-hSyn-DIO-TVA66T-dTom-CVS-N2cG virus (titer = $5.46x10^{12}$ vg/mL) was injected into L2/3 of S1 in the left hemisphere (1.1 mm posterior to bregma, 3.3 mm lateral, 300 µm deep) via iontophoresis at 5uA for 5 min. Four weeks later, 500 nL of EnvA-CVS-n2c(dG)-histone-EGFP virus (titer = $5x10^9$ vg/mL) was injected into S1 using the coordinates above via nanoinject.   Animals were sacrificed after 7 days.

Ex vivo **tissue preparation.** At the conclusion of *in vivo* imaging experiments, the cranial window was removed. Several small punctures were made in tissue surround the *in vivo* imaged area using a glass pipette dipped in lipophilic dye (SP-DiIC$_{18}$(3) (1,1'-Dioctadecyl-6,6'-Di(4-Sulfophenyl)-3,3,3',3'-Tetramethylindocarbocyanine; Fisher Scientific, cat no. D7777). Punctures were made in an asymmetrical pattern such that the orientation of the slice could be determined based on their

4

locations. A stereoscopic image was taken of the punctures relative to blood vessels. The animal was then euthanized and transcardially-perfused using 1X PBS followed by 4% paraformaldehyde (PFA; 32% stock (wt/vol); Microscopy Sciences, cat. no. 15710-S). The brain was removed and further fixed in 4% PFA overnight at 4^0C. The following day, the brain was mounted in 1.5% agarose gel (Agarose Molecular Bio Grade (100g); IBI Scientific, cat. no. IB70040) and sliced tangentially, parallel to the imaging plane in 150-300 um sections using a vibratome (Leica VT1000S Vibratome; Leica Biosystems). Slices were cleared using PACT-CLARITY procedure previously described(*14, 19*) For input mapping experiments, three or four 150 μm-thick coronal slices from each animal centered around the injection site were selected for further processing.

Probe set and barcode design. HCR-FISHv3.0 probe sets consist of a target sequence that binds to mRNAs of interest paired with one of three orthogonal HCR hairpin amplifiers (B1, B2, B3) conjugated to either AlexaFluor488, AlexaFluor546, AlexaFluor647, AlexaFluor750, AlexaFluor790(*56*) (Molecular Instruments, Inc.). Target binding sequences for transcripts were determined from sequences deposited in NCBI RefSeq (www.ncbi.nlm.nih.gov/refseq/) with the exception of RCaMP1.07 obtained from(*20*). Order and lot numbers for all probe sets are listed (**Supplementary Table 1**). Genes selected for cell type identification were determined empirically. From the scRNAseq data, candidate genes with a high degree of selectivity and penetrance were selected to provide maximal coverage to positively identify subclasses or cell types. Those with relatively high expression levels were prioritized to increase chances of detection with HCR-FISH. All candidates were then tested using HCR-FISH in tissue sections. Only those that could reliably be stained and visualized were ultimately chosen for inclusion.

For behavior experiments, a barcode scheme was implemented for gene readout based on a Hamming code similar to as previously described(*12*). The barcode contained two readout channels (B1-647 and B2-488). Readout of one gene was assigned to only one channel and encoded in two out of five rounds of staining. For error-robust encoding, a Hamming distance of 2 was used such that at least 2 errors were required to switch from one readout to another. For cellular-resolution readout, genes were assigned to readouts such that no co-expressed genes were present within one round and channel of staining. A sixth round of staining was added to confirm the identity of excitatory neurons using *Slc17a7* in B2-488 and inhibitory neurons using *Gad2* in B1-647. For registration and alignment of neurons across *in vivo* images and multiple round of HCR-FISH, probe sets for RCaMP1.07 in B3-546 was used across all staining rounds.

For input mapping and bilateral whisker deprivation experiments, fewer genes were read out and *Fos* mRNA was quantified in fosGFP animals. For these reasons, sequential multiplexed HCR-FISH of non-overlapping probes was performed instead of using overlapping probes as in the barcode scheme. Since GFP was expressed in both sets of tissue, readout of gene expression was used performed with B2-647 and a mixture of B1-750:B1-790 (1:1). Genes identifying cell types were selected based on results from single cell RNA sequencing of mouse S1 neurons using SMART-Seq v4 and 10x Genomics Chromium platform as previously described (portal.brain-map.org/atlases-and-data/rnaseq).

Multiplexed hybridization chain reaction fluorescent *in situ* hybridization. HCR-FISH was performed with modifications to the v3.0 protocol(*13*). Fixed, cleared samples were incubated in 500 µL of 30% probe hybridization buffer (30% formamide, 5x sodium chloride sodium citrate (SSC), 9 mM citric acid,0.1% Tween 20, 50 µg/mL heparin, 1x Denhardt's solution, and 10% low MW dextran sulfate) at 37^0C for 30 minutes. Samples were then moved to probe solution

overnight, which comprised of 500ul of 30% probe hybridization buffer and 2 µL of initiator probes (1 µL of odd probe and 1 µL of even probe, taken from 2 µM probe stock solutions) at 37^0C. The next day, samples were washed four times at 37^0C for 30 min in 500 µL of the following solutions, respectively: 75% probe wash buffer + 25% 5x SSC (Sigma Aldrich), 50% probe was buffer + 50% 5x SSC, 25% probe wash buffer + 75% 5x SSC, and 100% 5x SSC. Samples were then moved to 500 µL of amplification buffer (5x SSC + 0.1% Tween 20 + 10% low MW dextran sulfate) at RT on a shaker for 30 minutes. 10 µL of 3 µM stock hairpin amplifier solution was snap cooled by heating to 95^0C for 90 seconds and then allowed to cool in a dark drawer for 30 min. 10µL of both snap-cooled odd and even hairpins were added to 500 µL of amplification buffer to form the final amplification solution. Samples were moved to final amplification solution and allowed to amplify at RT overnight. The following day, samples were removed from the amplification solution and washed in 5x SSC three times at RT: 30 minutes, 30 minutes, and 15 minutes. Between staining rounds, *in situ* probes were removed using DNAse (Dnase I recombinant; Sigma Aldrich ct. no. 04716728001) as described(*15*). Samples were incubated for 30 min at RT in 500 µL of 1X incubation buffer (40 mM Tris-HCl, 10 mM NaCl, 6 mM MgCl2, 1 mM CaCl2). Samples were then moved to 500 µL of 1X incubation buffer with Recombinant DNase I (10 U/µL) for 4 hours at RT. Samples were then washed three times for 30 minutes at RT in 500 µL of MT Probe Wash Buffer. For bilateral whisker deprivation experiments, cell nuclei were stained using DAPI during the first round of HCR-FISH staining (DAPI Fluoromount-G; SouthernBiotech).

Confocal imaging. Tissue sections were mounted on 75mm x 25 mm glass microscope slides (Fisher Scientific) with Fluoromount-G (SouthernBiotech) and 50mm x 22mm cover glass (Fisher Scientific). Images were acquired on one of two confocal systems: 1) a Nikon C2+ Si spectral laser scanning microscope (LSM) with Nikon Plan Apo λ 20x/0.8NA, air objective, and 0.4094x0.4094x1 µm^3 XYZ image voxel size, or 2) a Nikon Ti2-E body with Yokogawa Spinning Disk and Nikon CFI Apo LWD 40x/ 1.15NA, water immersion objective, and 0.1625x0.1625x0.4 µm^3 XYZ image voxel size. Only one system was used across multiple imaging rounds for a given tissue sample. For LSM-acquired images, a single image volume was sufficient to cover the *in vivo* imaging region. For spinning-disk-acquired images, multiple image tiles spanning the *in vivo* imaged region were acquired and later assembled using TeraStitcher(*57*). For 'post-cleared' tissue prior to HCR-FISH staining, SP-DiIC$_{18}$(3) and endogenous RCaMP1.07 expression was acquired using 488 and 561 imaging channel, respectively. For HCR-FISH stained tissues, 488, 561, 647, or 785 imaging channels were used to visualize readout hairpins. DAPI staining was acquired using the 405 imaging channel.

Ex vivo **image analysis.** In order to re-identify neurons imaged *in vivo* and across multiple rounds of HCR-FISH, all acquired images were registered to a common reference image volume. First, 2D frame-averaged structural images taken from the behavioral session were registered into an *in vivo* two-photon 3D image stack using landmark-based 2D affine transformation (MATLAB). Next, one round of HCR-FISH staining was designated as the common reference image volume. The *in vivo* volume including registered behavior sessions, 'post-cleared' volume, and all other HCR-FISH volumes were then registered to the reference image volume based on endogenous protein or HCR-FISH stained mRNA RCaMP1.07 expression. Landmark-based 3D thinplate registration was performed to generate a coarse alignment of the image volumes using custom software (Neurotator). This coarse alignment produced a registration accuracy of <5µm. For

HCR-FISH stained volumes, thinplate registration was performed on the 561 imaging channel containing RCaMP1.07 expression was then applied to the remaining image channels. (**Fig. S1**). For input mapping experiments, HCR-FISH stained volume registration was performed on the 488 imaging channel containing GFP expression of input neurons.

Following coarse alignment, an automatic fine-scale 2D rigid alignment was applied to each z-frame of HCR-FISH stained volumes using matrix-multiply discrete Fourier transform(*58*). Registration was performed on the 561 imaging channel for behavior and bilateral whisker deprivation experiments or the 488 channel for input mapping experiments and then applied to the remaining image channels. For LSM-acquired images, fine-scale alignment was performed on the entire image stack. For spinning-disk-acquired images, sub-volumes corresponding to regions containing individual neurons imaged *in vivo* were first isolated and then subjected to fine-scale alignment in order to reduce CPU processing time.

In order to characterize gene expression in identified neurons, 3D cell segmentation was performed on image volumes. For behavior experiments, segmentation was performed using RCaMP1.07 expression. Following fine alignment, image stacks of RCaMP1.07 transcript expression across all imaging rounds were merged into a single volume stack. Segmentation was performed on the merged volume stack to obtain a single 3D segmented *ex vivo* ROI applied to each imaging round. For LSM-acquired images, segmentation was performed on HCR-FISH stained somatic RCaMP1.07 using Modular Interactive Nuclear Segmentation(*59*). For spinning-disk-acquired images, images stacks were pre-filtered to normalize signal intensity and to label nuclei within RCaMP1.07-expressing neurons using 3D Weka Segmentation(*60*). The resulting filtered images were merged with the original images and then segmented using Baxter Algorithm(*61*). For whisker deprivation experiments, segmentation was performed on DAPI stained nuclei. The resulting ROI was expanded radially by 10 voxels to better encompass the somatic region. RCaMP1.07 fluorescence within each ROI was use determined to determine whether identified cells expressed RCaMP1.07. For input mapping experiments, segmentation was performed on nGFP expression. The resulting ROI was expanded radially by 10 voxels to better encompass the somatic region. All *ex vivo* segmented neurons were manually validated using Neurotator.

Segmented *in vivo* ROIs were matched with segmented *ex vivo* ROIs by a combination of point cloud registration of ROI centroids and pixel overlap. Candidate matches were identified by nearest neighbor sorting (MATLAB). Overlap was calculated as:

$$2)\ overlap = \sqrt{overlap_{invivo}^2 + overlap_{exvivo}^2}$$

where $overlap_{invivo}$ is the fraction of *in vivo* ROI pixels overlapping with the *ex vivo* ROI and $overlap_{exvivo}$ is the fraction of *ex vivo* ROI pixels overlapping with the *in vivo* ROI. Candidate matches were rejected if $overlap < 0.5$. Matching ROIs were manually validated using Neurotator. *In vivo* imaged ROIs determined not be contained within the *ex vivo* tissue volume were assigned to be 'incomplete' neurons and excluded from cell type identification.

For behavior experiments, binary readout of gene expression in each HCR-FISH imaging round was visually scored by three human annotators through consensus using Neurotator. For decoding, barcodes were designed to avoid overlapping gene expression for each round of staining. Neurons missing at least one HCR-FISH imaging round were assigned as 'incomplete' and excluded from cell type identification. However, cells that co-express genes assigned to the same

imaging channel can occasionally produce ambiguity in decoding. To resolve these situations, a combinatorial list of candidate barcodes was listed based on the barcode scheme used in the experiment and all possible gene expression patterns. From this list, non-unique barcodes were excluded as well as barcodes in which exhibitory and inhibitory markers were co-expressed. Co-expressed genes were identified from this plausible list of barcodes. Any cells with ambiguous barcodes were assigned as 'undecoded' neurons and excluded from cell type identification. While the use of a Hamming code enables error correction of the barcode readout, no error correction was performed.

For input mapping and bilateral whisker deprivation experiment, the Python library *starFISH* was implemented for single mRNA spot detection and quantification(*62*). Spots were detected using *min_sigma* = 0.5, *max_sigma* = 7, and *num_sigma* = 15. Spot detection threshold was set using Otsu's method from the *scikit-image* library. Spot detection performance was verified visually. The number of spots were quantified within each ROI and expression levels were expressed as the number of spots per μm^3. For each round of staining, background spot density was quantified from the surrounding neuropil across tissue subvolumes and binary readout was determined if the ROI spot density exceeded 2 times the 95th percentile of background spot density.

Cell types were identified using gene expression patterns. While inhibitory classes and subclasses are identified by largely non-overlapping genes, excitatory cell types were identified by combinatorial expression patterns as follows:

$$3)\quad Adamts2 \Rightarrow (Fst \cup Ngb) \cap \neg (Penk \cup Rrad \cup S100a6 \cup Coch)$$
$$Baz1a \Rightarrow (Penk \cup Rrad) \cap (Fst \cup Ngb \cup S100a6 \cup Coch)$$
$$Agmat \Rightarrow (S100a6 \cup Coch) \cap \neg (Penk \cup Rrad \cup Fst \cup Ngb)$$

where $\cap$ = "and", $\cup$ = "or", and $\neg$ = "not." Neurons whose genes could not be coded or whose gene did not conform to these expression patterns were assigned as 'undecoded' neurons and excluded from cell type identification (see also **Text S1**).

For input mapping experiments, the density of input neurons along L2/3 was calculated as the number of nGFP+ cells within a 100μm sliding window along laminar depth or laterally from the injection site divided by the total number of nGFP+ cells within L2/3 for each imaged coronal slice.

Analysis of stimulus- and behavior-related activity. To assess the link between neuronal responses and various explanatory variables, a Poisson GLM was fit to each neuron's deconvolved train of calcium events across a recording session(*25*) (see also **Text S3**). The model defines probability in terms of a time-varying calcium event rate, λ_t, given by:

$$4)\quad \lambda_t = \exp\left(\sum_i w_i x_i(t)\right)$$

where $x_i(t)$ represents the time course for the ith explanatory variable, and w_i represents the effect of this variable on the neuron's probability of spiking(*63*). The regularized log-likelihood of a calcium events for an individual trial, assuming a Poisson distribution, is given by:

$$5)\quad \log p(r|x,\theta_w) = \sum_{t=0}^{T} r_t \log \lambda_t - \Delta \sum_{t=0}^{T} \lambda_t + \gamma \|w\| + C$$

where Δ is the time bin size, T is the number of time bins in the trial, r_t is the calcium event at time t, and γ is the lasso penalty term which encourages sparseness on the weights, w. All GLMs were fit using MATLAB's lassoglm function with a Poisson link function, 6 penalty values (γ), and 4 fold cross-validation.

To represent the time-course of task variables $x_i(t)$, boxcars were constructed which were designated as "true/1" during time-periods of interest and "false/0" elsewhere. Since task timing was fixed across trials, each trial could be broken up into six time-periods of fixed start time and duration: "pre", "sample", "early delay", "late delay", "test", and "report". Complementary covariates were represented as independent boxcars (ie. anterior stimulus and posterior stimulus; match and non-match; lick and no lick) to capture any asymmetry in the neuron's response. To assess if a neuron's activity could be explained by trial information occurring at multiple points in the trial, some task variables were represented in multiple time periods. For a given trial, the sample stimulus direction was represented as three boxcars: during the sample stimulus presentation period, during the early delay period, and during the late period. Trial category and choice were represented as a boxcar during both the test period and the report period.

Whisker kinematics and population activity were represented as continuous variables across the entire trial. All whisker kinematic features were z-scored and down-sampled to the imaging rate before including as a covariate. Whisker touch onset and offset was represented as a boxcar of width 5 bins (150 ms) centered at the touch event. The coupling covariate was calculated for each neuron by excluding the given neuron's calcium events, then calculating the non-negative matrix factorization (NMF) of the matrix of calcium events of all other neurons in the session(*26*). A NMF of rank = 1 used when assessing encoding of task factors. For assessing coupling across varying NMF ranks, each rank was included as a covariate in the model and the coupling factor included all covariate ranks.

Related covariates were grouped together into 'task factors.' For each task factor, a partial model was constructed that excluded the covariates associated with this task factor. Any increase in deviance from the full model to the partial model therefore resulted from the exclusion of this task factor's covariates. Akaike Information Criterion (AIC) was used to compare deviance between partial models in which different number of covariates were excluded such that:

$$6)\ AIC = 2k - 2\ln(L) = 2k + deviance$$

where k is the number of model parameters, deviance $= -2\ln(L)$, and L is the model likelihood. The difference in AIC (ΔAIC) between the full and partial model was calculated as:

$$7)\ \Delta AIC = AIC_{partial} - AIC_{full}$$

For analysis, three GLMs were constructed. Model 1 (task GLM) was constructed to assess task-related coding of neurons using task variables and task factors shown in **Fig. S10**. Model 2 (free whisking GLM) was constructed to assess neuronal responses to free whisking. Only whisker kinematic covariates included in Model 1 were included in this model. Task factors were calculated for each of these covariates. The model only included time points consisting of the last 1.4 s prior to sample period touch onset and the last 1.1s prior to test period touch onset, consistent with periods of no whisker-rotor contact preceding stimulus presentation.

Model 3 (cell type coupling GLM) was constructed to assess coupling of activity of each major cell subclass or type and consisted of all task variables in Model 1 with the exception of the

'coupling" covariate for all simultaneously neurons. Instead, seven coupling covariates for the six main cell populations (Adamts2, Baz1a, Agmat, Pvalb, Sst, Vip) and all other, unlabeled (UNL) cells consisting of those assigned to be 'incomplete' or 'undecoded' were included and consisted of the NMF of rank = 1 of the calcium events for simultaneously recorded neurons sorted according to each cell subclass or type. Task factors in this model corresponded to each of the main cell type coupling covariates.

For bilateral whisker deprivation experiments, the mean event rate to anterior and posterior whisker deflections was calculated. To account for direction selectivity, the maximum activity level to either stimulus direction was used as measure of a neuron's stimulus response (SR). The change in stimulus responsiveness during BD was expressed as $(SR_{post} - SR_{pre})/(SR_{post} + SR_{pre})$ where SR_{post} is the stimulus response at either day 1 or day 5 and SR_{pre} is the mean stimulus response across Day -2,-1, and 0. We calculated a neuron's response reliability (RR) by first separately calculating the fraction of trials in which a neuron produced a calcium event for either anterior or posterior whisker deflections and then taking the maximum between two stimuli in order to control for direction selectivity. The change in response reliability during BD was expressed as $(RR_{post} - RR_{pre})/(RR_{post} + RR_{pre})$ where RR_{post} is the response reliability at either day 1 or day 5 and RR_{pre} is the mean stimulus response across Day -2,-1, and 0.

Network analysis. Network analysis was performed to analyze functional connectivity between cell types across different task conditions. Task-specific networks were constructed, composed of neurons exhibiting significant ΔAIC ($P < 0.01$, χ^2 test) to task factors in Model 1 (task GLM). A 'non-coding' network was composed of neurons that did not exhibit any significant coding for any the task variables. Information contained in each network was derived from results from Model 3 (cell type coupling GLM). A network contained six nodes that were each composed of neurons belonging to a given major cell population. An input node was defined as the neuron modeled in the cell type coupling GLM. An output node was defined as the cell types coupling factor explaining the activity of the modeled input neuron node. A directed network edge from the output node to the input node was defined as the ΔAIC of a particular cell type coupling factor that explains the activity of the input node, averaged across all input node neurons.

Network strength was calculated as the mean edge weight for all edge weights in the network. The input node strength was calculated as the sum of weights of inward directed edges from output node to the input node divided by the number of inward directed edges. The output node strength was calculated as the sum of weights of outward directed edges from input node to the output node divided by the number of outward directed edges. To test the strength and stability of functional connections across task conditions, the overall connection strength was calculated as the mean edge weight across all task networks. The stability of the connection was calculated as the coefficient of variation of the edge weight across all task networks. To test whether network strength correlated with spatial clustering of cell types *in vivo*, the mean centroid distance between all pairs of neurons for a given pair of cell types were calculated from *in vivo* images.

Statistical procedures. No statistical methods were used to predetermine sample size. The experiments performed were not randomized and the investigators were not blinded to allocation during experiments and outcome assessment. Statistical tests used are indicated in figure legends. Error bars on plots indicate standard error of the mean (s.e.m.) unless otherwise noted.

For statistical tests of task encoding, a χ^2 test was performed to assess the significance of the positive GLM ΔAIC values. A Mann-Whitney U test was used to compare the strength of

GLM ΔAIC values between cell types. The Bonferroni-Holm method was used to correct for multiple comparisons.

For statistical tests of bilateral whisker deprivation, a one-way ANOVA test with post-hoc multiple comparison test was used to assess change in stimulus response across the imaging sessions. A Student's t-test was used to assess differences in stimulus response between fosGFP neurons as well as between excitatory cell types. A χ^2 test was used to compare fraction of stable high-expressing fosGFP cells between excitatory cell types. Standard deviation of the fraction of stable high-expressing fosGFP cells for a given cell type was obtained by bootstrapping with replacement. The fraction of stable high-expressing fosGFP cells was determined from subsets (60% of total) of cells that were randomly sampled with replacement. This process was repeated 1,000 times and the standard deviation was determined from this distribution.

For statistical tests of network analysis, to determine whether a given node strength was significantly different from nodes within the same network or between networks, bootstrap sampling with replacement was performed on the neurons representing the network. The edge strengths and node strengths were recalculated from the resulting bootstrapped data set. This process was repeated 1,000 times to obtain 95% confidence intervals for significance tests. The original node strength was then compared to the bootstrapped node strength of the other nodes in the same network or the same node across networks for within- or across-network comparisons, respectively. To determine whether a given connection was stronger and more stable than chance, permutation tests were performed by shuffling cell type labels for each input node for each task network and recalculating the overall connection strength and stability. This process was repeated 1000 times to obtain a shuffled distribution. Connections that were both stronger and more stable than the 95th percentile of the shuffled distribution were considered to be above chance. To determine whether cell types imaged *in vivo* were more spatially clustered than chance, permutation tests were performed by shuffling cell type labels and recalculating the pair-wise distance between cell bodies. This process was repeated 1000 times to obtain a shuffled distribution. Distances less than 5th percentile of the shuffled distribution were considered to be above chance. The Bonferroni-Holm method was used to correct for multiple comparisons. For statistical tests of input mapping, a one-sided Student's t-test was used to assess higher sublaminar and cell type differences in input density between Vip and Sst classes.

Supplementary Text
S1. Sampling of Neurons with the CRACK platform
In principle, the CRACK platform offers an unbiased survey of cell type-specific functional responses across a neuronal population. A few factors should be considered when planning experiments, assessing the accuracy of cell type readout, and comparing the proportion of cell types across studies. When comparing barcode readout vs. sequential readout at cellular resolution, barcode readout provides higher read depth in fewer labeling rounds but requires that genes with non-overlapping expression patterns be selected for cell type identification. Depending on the barcode design, cells with co-expression of multiple overlapping genes may not be decoded and identified. In this study, identification of Baz1a neurons required the co-expression of at least two genes (see **Methods**). However, expression of more than two genes that fit the cell type criteria were also observed (**Fig. S4C**). This suggests that the use of barcode readout in the behavior experiments could result in Ba1za neurons with co-expression of multiple (4-6) identifying genes to be undecoded (**Supplementary Table 2**). Under these circumstances, using barcode readout with single molecule mRNA resolution may help to resolve the identities of these cells. Bilateral deprivation and input mapping experiments employed sequential readout because fewer cell types (and therefore genes) were assayed and GFP expression restricted the use of the 488 imaging channel for labeling mRNA transcripts. These experiments enabled the ability to identify Baz1a neurons with co-expression of multiple identifying genes that could not be decoded in the barcode scheme at cellular resolution.

In this study, task responses of neuronal cell types were restricted to neurons expressing RCaMP1.07 that were observed to be active during the imaging session. The relative number of active RCaMP1.07+ neurons in each subclass or cell type was observed to be disproportionate to previously measured cell type distributions in L2/3 S1(*7, 10, 36, 42*) (**Supplementary Table 2**). RCaMP1.07 was expressed virally using an AAV with PhP.eB serotype(*64*). The tropism of AAV serotypes has been shown to preferentially infect certain neuronal cell types(*65*). We assessed the distribution of RCaMP1.07+ neurons in control tissue across cell types stained with HCR-FISH (**Fig. S3**). Overall, we observed that AAV.PhP.eB had a higher likelihood of infecting excitatory neurons over inhibitory neurons. For inhibitory neurons, the tropism of the AAV.PhP.eB produced an under-representation of Pvalb and Vip class neurons compared to Sst class neurons. Whether this under-representation is stochastic or specific to certain Pvalb or Vip subclasses remains to be determined. In the future, the use of pan-neuronal transgenic lines will alleviate potential biases could result from viral tropism.

Neurons in the calcium imaging data were automatically segmented using a constrained nonnegative factorization (CNMF) approach(*54*). This approach identifies neurons that exhibit active calcium responses. The activity levels of these automatically segmented neurons are shown (**Fig. 2G, Fig. S13A, S15A**). Neurons identified as potentially inactive can be either interpreted as non-spiking neurons or those whose calcium signal-to-noise levels were not sufficient to be segmented using CNMF. The number of identified active and inactive neurons within the imaging field of view were quantified (**Supplementary Table 2**). Some cell type differences were observed. For example, Baz1a neurons were more likely to be identified as active than other excitatory cell types which is also consistent with the higher event rates of active Baz1a neurons. Taken together, the results indicate choice of viral tropism and activity-based segmentation algorithms can influence sampling of neurons.

In comparing cell type distributions obtained from CRACK with other methods, there are two considerations. First, cell type distributions obtained from FISH are not comparable to

distributions obtained from scRNAseq. Cell type-specific differences in survival during cell isolation for scRNAseq can affect the relative proportions(*1*). Tissue dissection also provides limited spatial resolution to resolve sublaminar differences in cell type distributions and can also capture cells from a mixture of layers. Thus, it is more appropriate to compare cell type distributions with other studies using FISH(*66*). Second, tissue section orientation should be considered when analyzing cell type distribution. Whereas coronal and sagittal sections facilitate the analysis of sublaminar cell type distributions, tangential sectioning to aid in *in vivo* to *ex vivo* registration can often obscure laminar cytoarchitecture. Thus, it is important that tissue depth in tangential sections be tracked if cell type distributions at specific laminar positions need to be measured.

S2. Comparison of Calcium Responses and Event Detection across Cell Types
In the CRACK platform, two-photon calcium imaging is critical for monitoring functional responses of neurons in a manner that is compatible with post-hoc multiplexed FISH. Since calcium transients are a surrogate for spiking activity, calcium transients must be deconvolved before use in GLMs to more accurately characterize response patterns at timescales relevant to behavior. Methods to infer spike-related calcium events using deconvolution rely on calibration experiments involving simultaneous electrophysiology and calcium imaging as well as an understanding of the response properties of the calcium indicator and biophysical properties of calcium within neurons. In this study, calcium responses were deconvolved using an Online Active Set method to Infer Spikes (OASIS), a generalization of the pool adjacent violators algorithm (PAVA) for isotonic regression(*67*) (**Fig. S8A**). The extent to which the relationship between action potential and calcium events varies across cell types and how OASIS accommodates this variability is an open question. Calibration experiments in inhibitory classes using the indicator GCamp6f show that calcium responses in Pvalb neurons can underestimate spiking activity compared to Sst and Vip neurons(*11, 33*). Such calibration experiments are facilitated by transgenic labeling so that cell types can be selectively targeted. Currently, there are no transgenic lines that selectively label Agmat, Baz1a, and Adamts2 excitatory cell types.

Without the ability to obtain calibration data with RCaMP1.07 for all cell types investigated in the study, we focused solely on assessing cell type differences in the fluorescence signals (baseline fluorescence, noise levels, rise time, and decay time) that could potentially contribute to differences in calcium event inference using OASIS. Baseline fluorescence intensity (bottom 10th percentile of signal intensity) would reflect expression levels RCamp1.07 or resting calcium concentration (**Fig. S8D**). We found no differences between excitatory cell types. For inhibitory cell classes, Pvalb showed higher relative baseline fluorescence compared to other inhibitory classes ($P < 0.05$, two-tailed Student's *t*-test with Bonferroni-Holm post-hoc correction) potentially reflecting unique buffering capacities(*68*). No differences were observed in shot noise levels between cell types (**Fig. S8E**).

In OASIS, calcium event estimates rely on a convolution kernel consisting of exponential rise and decay time constants that are self-tuned for each cell using an autoregressive (AR) model. Since rise and decay times are modeled from the raw calcium data for each cell, this provides a generative method based on the AR model for comparing expected calcium kinetics across cell types. No differences in rise time were observed between cell types (**Fig. S8F**). Adamts2 cells show faster decay times than other excitatory neurons ($P < 1\times10^{-5}$, two-tailed Student's *t*-test with Bonferroni-Holm post-hoc correction) while Pvalb cells exhibited faster decay times compared to

other inhibitory neurons ($P < 0.05$, two-tailed Student's t-test with Bonferroni-Holm post-hoc correction; **Fig. S8G**).

To determine whether cell type differences in calcium response properties influenced calcium event detection inference, we examined the distribution of calcium events ($\hat{s}$) resulting from deconvolution. The magnitude of $\hat{s}$ relates to the confidence that $\hat{s}$ is a spiking event, with lower $\hat{s}$ values reflecting poorer estimates. The distribution of $\hat{s}$ extracted from a time series can be used to determine the performance of the auto-regressive model for a given cell. For each cell, we compared model performance by performing a receiver operating characteristic analysis across $\hat{s}$ values. In general, we found that lower noise levels and longer decay times were weakly correlated with better model performance (**Fig. S8C**). However, these relationships did not necessarily translate when comparing cell type differences. For excitatory neurons, model performance was better for Agmat neurons ($P < 1\text{x}10^{-5}$, two-tailed Student's t-test with Bonferroni-Holm post-hoc correction) and weaker for Adamts2 neurons ($P < 1\text{x}10^{-5}$, two-tailed Student's t-test with Bonferroni-Holm post-hoc correction; **Fig. S8H**). No differences were observed for inhibitory neurons. With the known exception of Pvalb neurons, we conclude that calcium response properties between cell types do not systemically differ in a manner that would result in differences amongst the other cell types when inferring calcium events using OASIS.

While OASIS is intended for spikes inference from calcium signals, since the exact calcium-to-spiking relationship is not known for each cell type, we do not interpret the deconvolved signals $\hat{s}$ as individual spikes but as a likelihood measure of a calcium event. Subsequently, these signals are thresholded into binary events for two reasons. First, to eliminate unreliable calcium events, any deconvolved signal that does not exceed the measured signal-to-noise ($\hat{s} < 1$) is thresholded to 0. Any deconvolved signal where $\hat{s} > 1$ is thresholded to 1 so that a GLM assuming a Poisson distribution could be used to model neuronal responses. Since $\hat{s} > 2$ could be interpreted as calcium events composed on multiple events, thresholding signals in which $\hat{s} > 1$ could underestimate calcium events. Analysis of the distribution of $\hat{s}$ demonstrates that with the sampling rate of imaging and the kinetics of RCamp1.07, occurrences of $\hat{s} > 2$ are rare and are thus unlikely to underestimate GLM model performance (**Fig. S8B**).

We asked whether calcium response properties and calcium event detection had any relationship to GLM performance. Across the analyzed neuronal population, we observed no correlation between overall GLM fit for the task encoding model and calcium signal noise level and only weak correlations when compared to calcium decay time, calcium rise time, and the calcium detection performance (**Fig. S10A**). This demonstrates that differences in calcium responses properties from which deconvolution was performed has minimal influence on GLM performance across individual neurons that would explain task-related differences across cell types investigated.

S3. Task Encoding Across Neurons

A GLM was used to assess the encoding of task-related responses in single neurons assuming a Poisson distribution of estimated deconvolved calcium events. Variables representative of trial type were represented as boxcars that spanned epochs of the trial period. Whisker kinematics and population activity were represented as continuous variables. While the use of kernels to form basis functions can capture the time-varying relationship between behavior events and the neuron's probability of spiking(*26, 69*), kernels were excluded in the GLM for a few reasons. Representing task variables through multiple kernels, substantially increases the number of covariates included in the GLM which increases the chance of model overfitting. While information about temporal

response properties are not captured in the task encoding model, these dynamics are not necessary for comparing the relative strength of task-related responses between cell types. Rather, the exclusion of kernel reduces model complexity and eases the interpretation of the model results.

The information content of a neuron's activity for a given task factor was determined by comparing the AIC of the full model containing the task factor against the AIC of the partial model which excluded covariates representing that task factor. We chose to use AIC to convey GLM fit because it is a principled way to compare fit between models of different complexity (i.e. different number of model parameters). AIC accounts for the trade-off between the goodness of fit (risk of overfitting with large number of model parameters) and simplicity (risk of underfitting with too few model parameters). ΔAIC reports the difference in model fit between a full model and partial model that is agnostic to model complexity. Statistical significance and ranking of models can be assessed using ΔAIC values, which enables information content to be compared both within and across different task factors and cell types. A χ^2 test was performed to assess the significance of positive ΔAIC values, interpreted as the neuron's activity encoding a given task factor. Neurons can exhibit 'mixed selectivity' in which they significantly encode multiple task factors (**Fig. S12**).

It should be noted that ΔAIC differs from deviance explained, a measure of the goodness of model fit by comparing the full model to the null model. Overall, 'non-coding' neurons where ΔAIC was not significant to any of the task factors showed poorer model fits compared to neurons encoding at least one task factor (**Fig. S10B**). We compared deviance explained for the full model against the ΔAIC of each task factor for each neuron (**Fig. S10C, S14B**). The majority of task factors were positively correlated with model fit. In particular, strong correlations with stimulus direction, whisker kinematics, and population coupling suggest that these task factors were key drivers of goodness of fit for the GLM used in this study. However, task factors for category and touch offset showed no significant correlation. This demonstrates that information content of a given task factor and goodness of model fit are not necessarily related. A neuron's activity can encode information about a given task factor while simultaneously having a poor overall model fit. Similarly, a neuron's event rate can correlate with task encoding (**Fig. S10D, S14B**) but not in a consistent manner across all task factors or cell types. This dissociation between event rate and task factor suggests a potential biological explanation underlying neurons with both high activity levels and task encoding rather than merely a statistical relationship captured by the GLM.

S4. Measuring Functional Connectivity using Cell Type Coupling
In order to assess how a neuron's activity relates to the surrounding population, the dimensionality of the population activity was reduced using non-negative matrix factorization as previously described(*26*). For analysis of population coupling in the task encoding GLM, the population activity was factorized into varying ranks. Ranks were defined as an individual covariate in the model and characterized as the functional response of non-overlapping subpopulations. The task factor for coupling consists of all of these rank covariates. We measured coupling as increasing number of ranks are included in the model (**Fig. 5A**) and observed that ΔAIC increases with the number of ranks. This means that as more of the variance in the population activity is captured in the GLM, neuron's activity can be better explained by the activity from these different subpopulations. For the cell type coupling GLM, the population activity was subdivided by cell type. Since subdividing by cell type reduces the number of neurons in each subpopulation, a factorization rank (r = 1) was used to standardize the population activity of each cell type.

Co-fluctuations in activity between neurons while controlling for stimulus and other task conditions ('noise correlations') are often used as a measure of functional connectivity of

neurons(*70*). In the cell type coupling GLM, we fit a neuron's activity to task variables as well as the cell type coupling covariates capturing the activity to each of the simultaneously recorded cell types. The covariate weights obtained in the GLM are similar to noise correlations. For illustration, we plot the weights of cell type coupling covariates for neurons that encode stimulus direction against the noise correlation across trials with the same stimulus condition (**Fig. S10**). As can be seen, positive or negative covariate weights typically correspond to positive or negative noise correlations.

Functional connectivity of a cell type is computed as the ΔAIC of the full model against the partial model excluding the cell type coupling factor. This calculation asks whether the co-fluctuations in activity that are observed can be explained by activity related to task variables or that of other neurons recorded in the population. Thus, a significant, positive ΔAIC identifies noise correlations that are specific to that cell type and cannot be explained by other recorded neurons. Positive or negative correlations can both produce a significant, positive ΔAIC.

A significant, positive ΔAIC value of a neuron's cell type coupling factor serves to reject the hypothesis that those input sources are not shared by the other recorded neurons since they would have been explained away by the other covariates. It can also raise two possible interpretations. The first interpretation is the presence of a direct synaptic interaction between the neuron and the cell type. The second interpretation is that the neuron and the cell type share common input from a source that is not captured in the population recording. This is because the ΔAIC can only explain the activity patterns from simultaneously recorded neurons included in the full model. This second interpretation may be applicable to functional connectivity between inhibitory cell types in which significant coupling weights are not negative as would be predicted from direct inhibition. For example, strong inhibitory interactions between Sst and Vip neurons can be identified when measuring subthreshold responses(*40*) but exhibit de-correlated, rather negatively correlated, trial-by-trial calcium responses under task conditions(*11*). Positive weights when considering inhibitory-inhibitory and excitatory-inhibitory functional connectivity could potentially be explained by excitatory drive from a non-measured source such as bottom-up input from L4 or thalamus or top-down input from high-order areas.

Functional connectivity analysis provides complementary insight into how cell types interact under task conditions. Our analysis of task networks show that cell types interactions are layered upon coding features of individual cells. Relative networks strengths between task networks may reflect differences in how such information is encoded locally versus inherited from other areas. For example, S1 is necessary for coding category information during behavior and neurons encoding such information exhibit strong interactions. In contrast, sample_LATE DELAY information is inherited from secondary somatosensory cortex where neurons encoding such information in S1 exhibit weak interactions(*24*). Labeling connections as strong and stable vs. weak and variable provides additional clues as to which connections may be stable, intrinsic motifs vs. transient, dynamic interactions. While certain cell types can be clustered with other cell types, their spatial proximity does not correlate with the strength of these functional connections (**Fig. S22C**). Ultimately, distinguishing between direct and indirect connectivity requires confirmation experiments to test synaptic connectivity (**Fig. 6**).
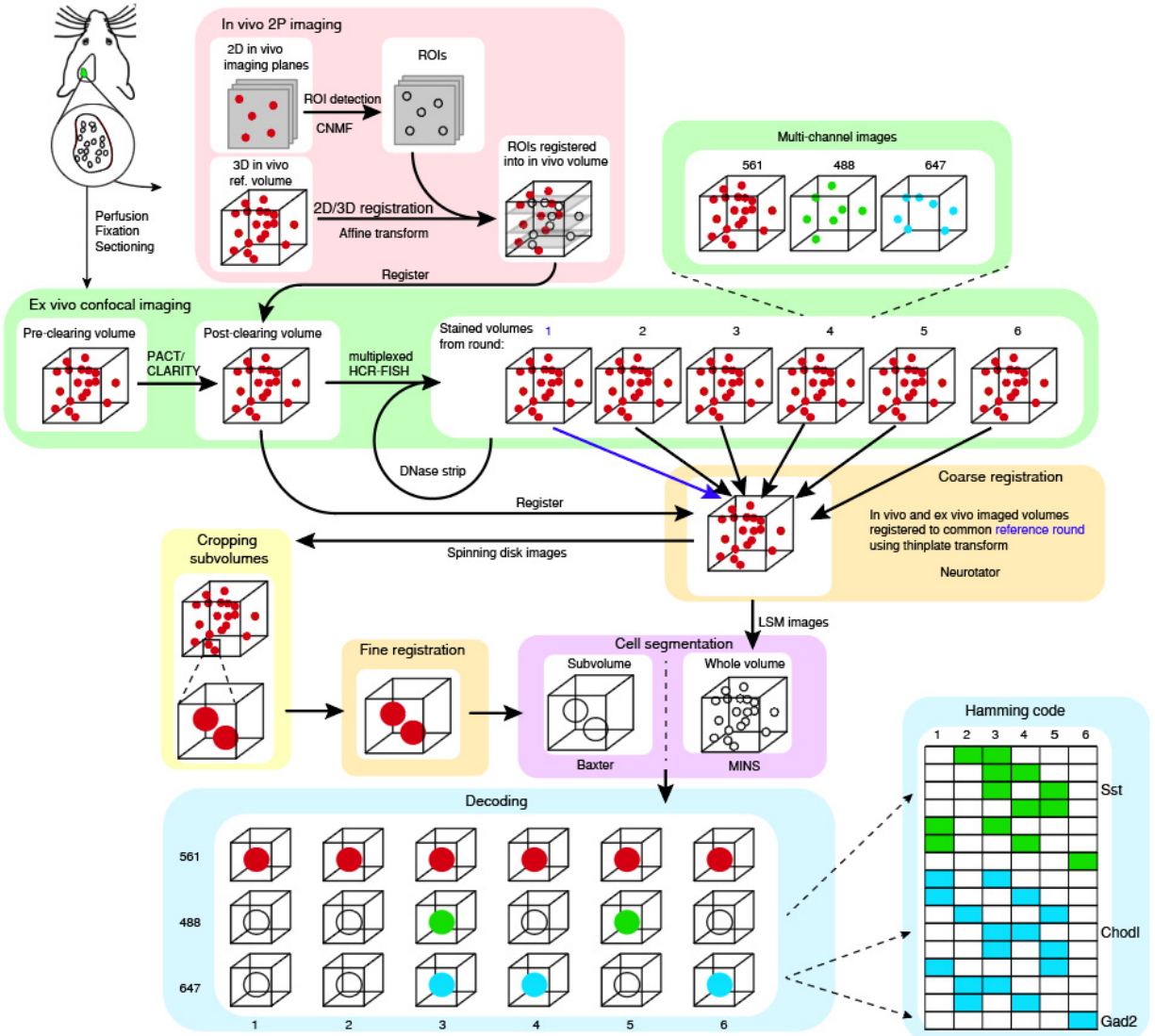
Fig. S1. CRACK platform workflow. *In vivo* two-photon calcium imaging of neuronal activity was performed during behavior. Two-dimensional regions of interest (ROIs) corresponding to active neurons were segmented and registered into an *in vivo* 3D reference stack. Following tissue extraction and clearing, *in vivo* area was re-identified and 3D confocal image volumes were acquired prior to and following multiple rounds of HCR-FISH staining. *In vivo* and *ex vivo* image volumes were coarsely registered to a common reference volume based on RCamp1.07 expression (561 channel). For LSM confocal images, 3D cell segmentation was performed on the entire imaging volume. For spinning disk images, imaging volumes were first cropped into sub-volumes, further subjected to fine alignment, and then 3D cell segmentation. Segmented *in vivo* and *ex vivo* ROIs are matched. HCR-FISH staining in the complementary channels (488 and 647) are decoded to obtain gene expression patterns.
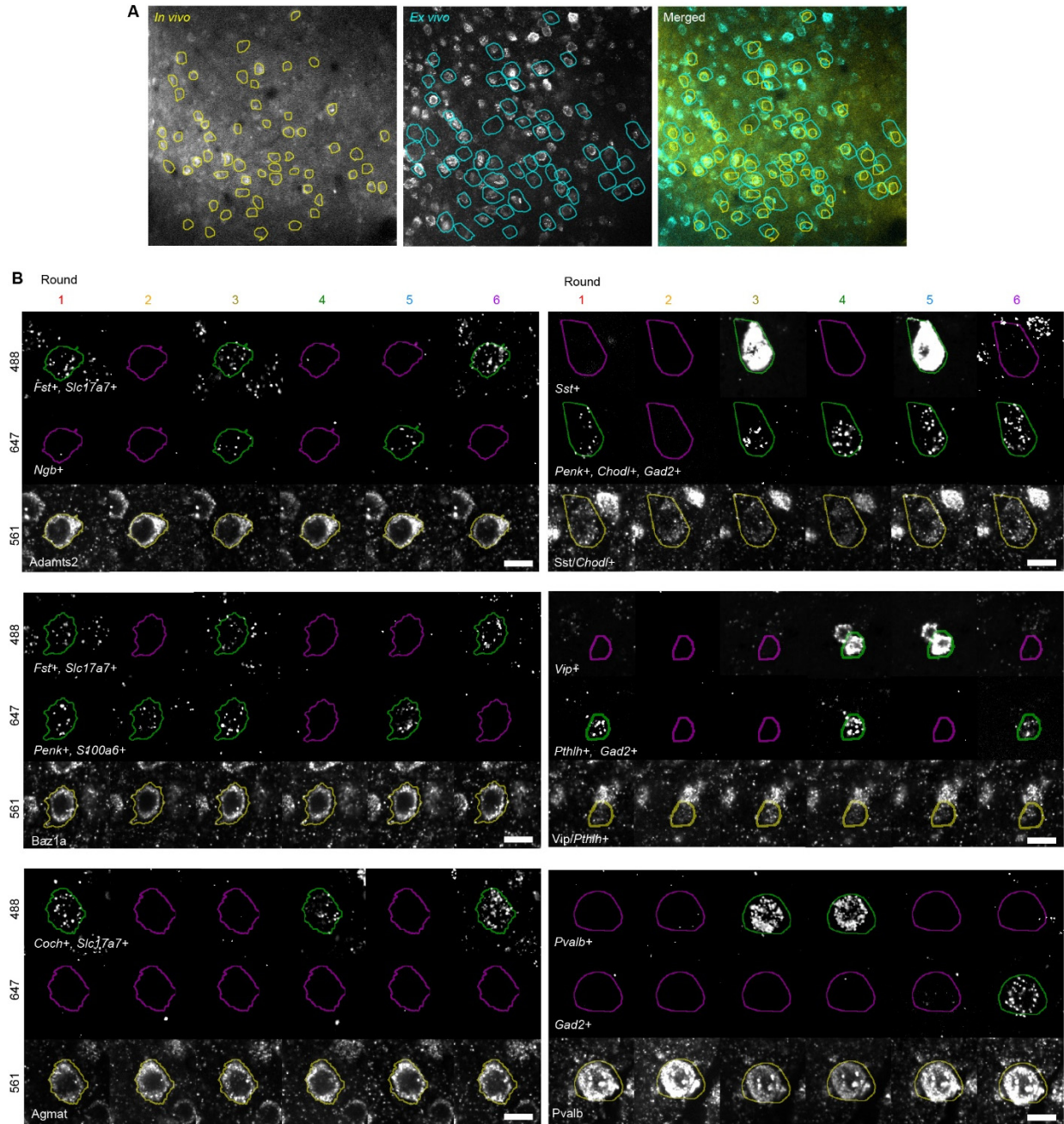
Fig. S2. Example cell registration and HCR-FISH barcode readout. (**A**) Example of cell registration between *in vivo* and *ex vivo* images. 2D cell segmented ROIs obtained *in vivo* from active neurons and overlaid on 3D cell segmented ROIs obtained from HCR-FISH labeling. (**B**) Examples of decoded types and subclasses from the barcode scheme in **Fig. 1C.** Individual HCR-FISH rounds are shown with *RCaMP1.07* expression for registration along with B2-488 and B1-647 readout channels. Visually scored positive (green) and negative (magenta) readouts are denoted for each channel and round in the segmented neuron masks. Scale bar: 20 μm.
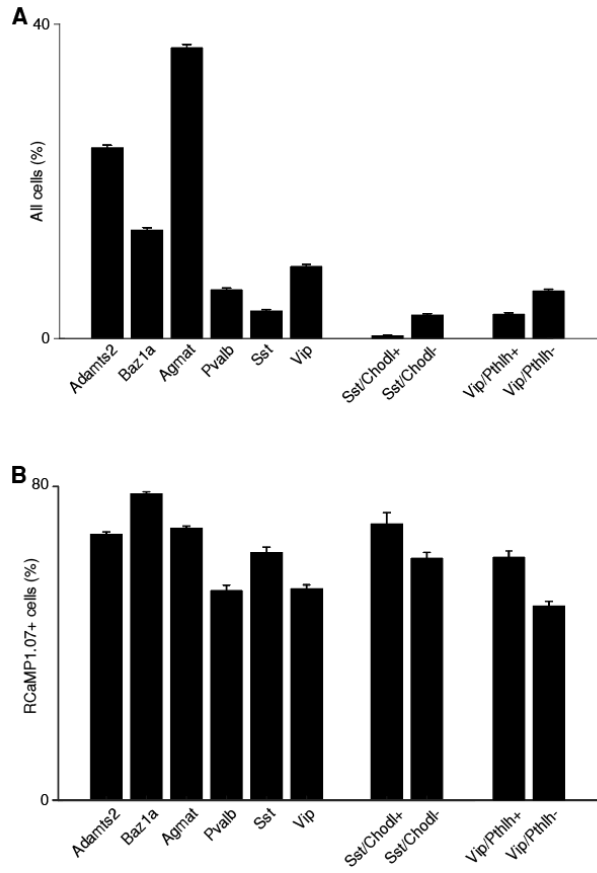
Fig. S3. Distribution of L2/3 cell types identified by multiplexed HCR-FISH. (**A**) Cell type proportions across all L2/3 neurons (RCaMP1.07+ and RCaMP1.07-) identified by multiplexed HCR-FISH. (**B**) Fraction of viral-mediated RCaMP1.07+ neurons identified by multiplexed HCR-FISH show preferential labeling of L2/3 cell types by AAV.PhP.eB vectors. Error bars; s.d. from bootstrap analysis. n = 11,100 neurons from 3 animals.
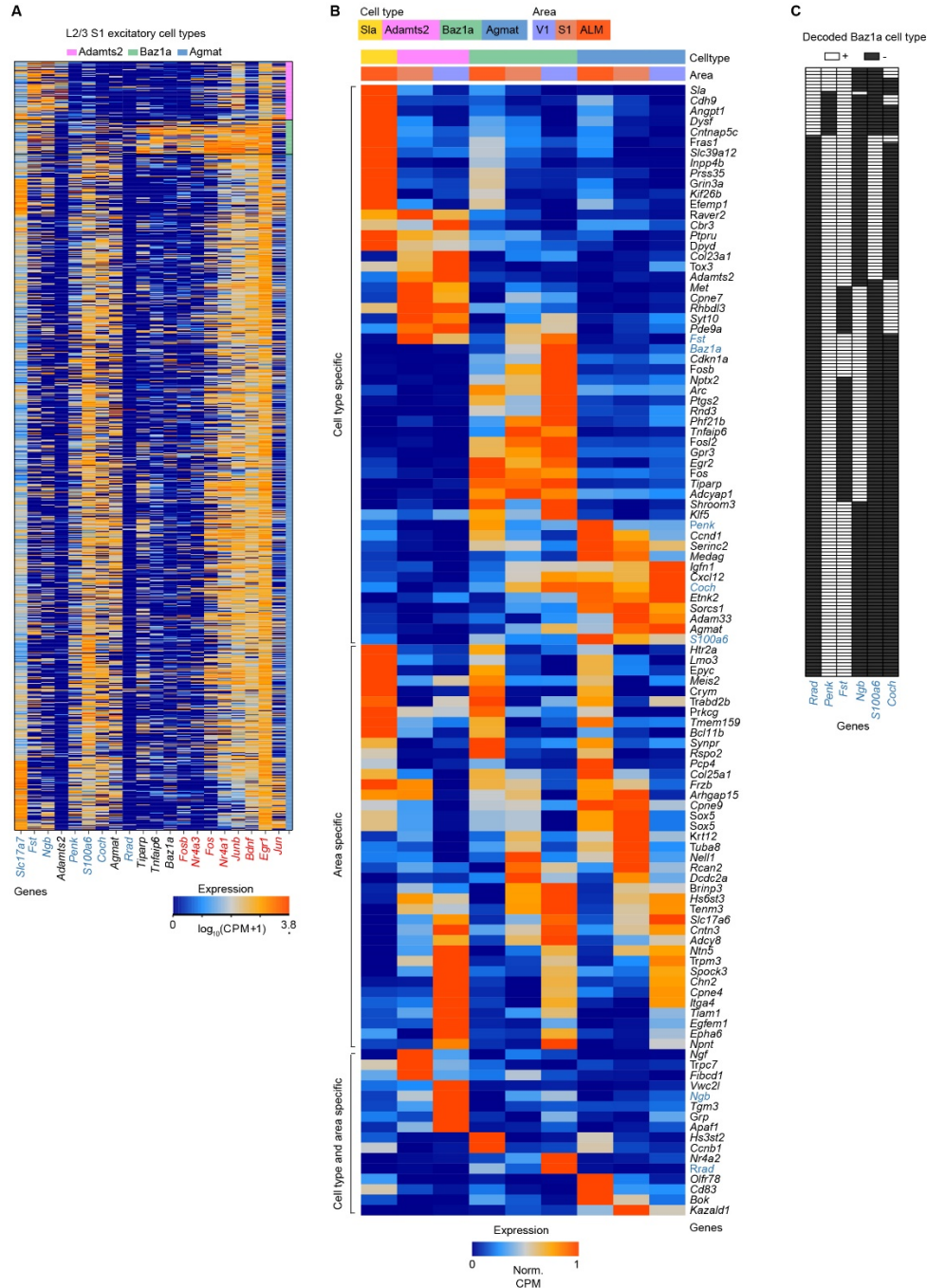
Fig. S4. Single cell RNAseq analysis of L2/3 excitatory cell types. (**A**) Three major molecularly defined excitatory types in L2/3 S1 identified by single cell RNA sequencing. Expression patterns of select genes for individual cells are shown. Genes used in the CRACK platform are denoted (blue). Baz1a neurons show selective expression of immediate early genes (red). Additional selective expression of non-immediate early genes (black) indicates that Baz1a is a static excitatory cell type. (**B**) Comparison of L2/3 excitatory cell types across S1, V1, and ALM. Genes with cell type specificity, area specificity, and both area and cell type specificity are shown. CPM, counts per million. (**C**) Expression profiles for decoded Baz1a cells from task behavior experiment.

20
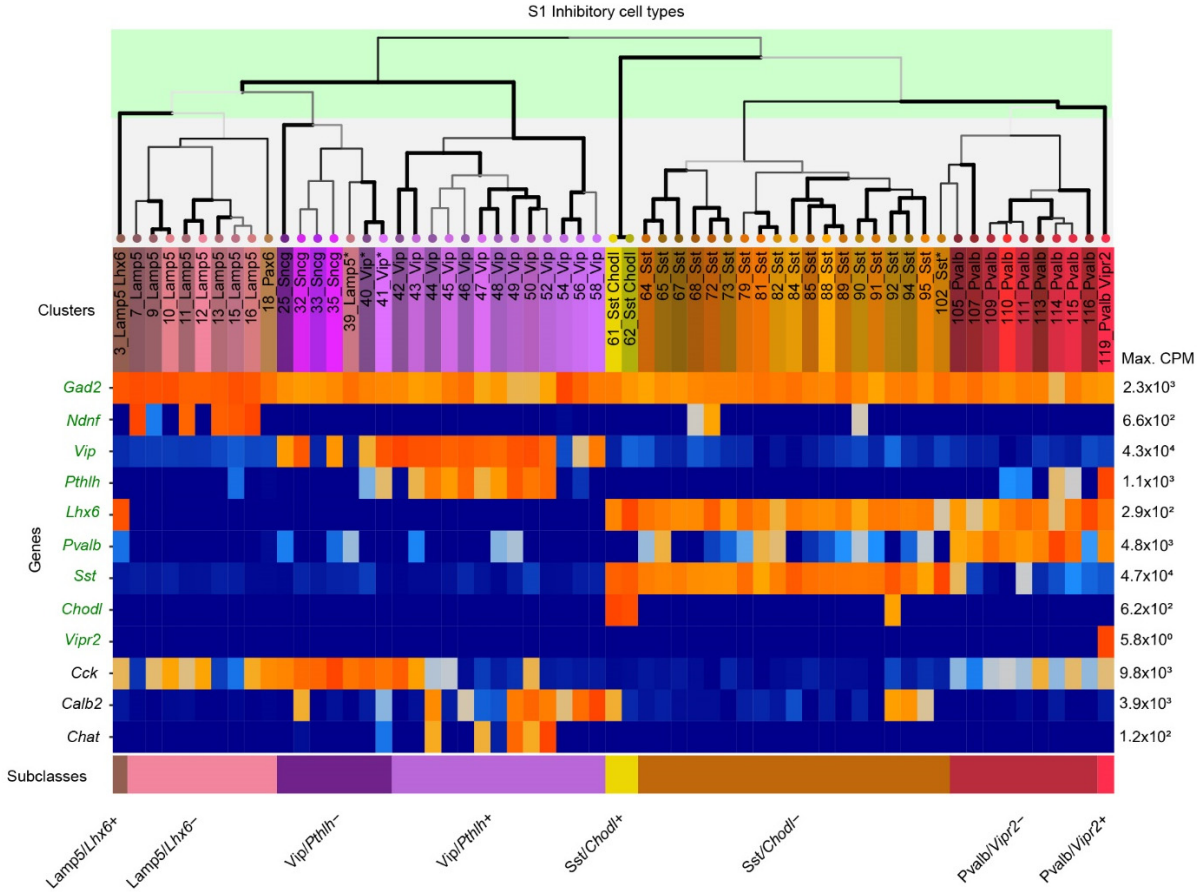
Fig. S5. Single cell RNAseq analysis of inhibitory subclasses. Dendrogram (top) depicts the hierarchical organization of inhibitory neurons into multiple discrete cell types. Expression profiles for a subset of genes including those selected for CRACK (green) are shown for each cluster (middle). Each gene is normalized to its maximum expression value. Selected subclasses and types for CRACK (bottom) correspond to the hierarchical level in the shaded green region of the dendrogram. CPM, counts per million.
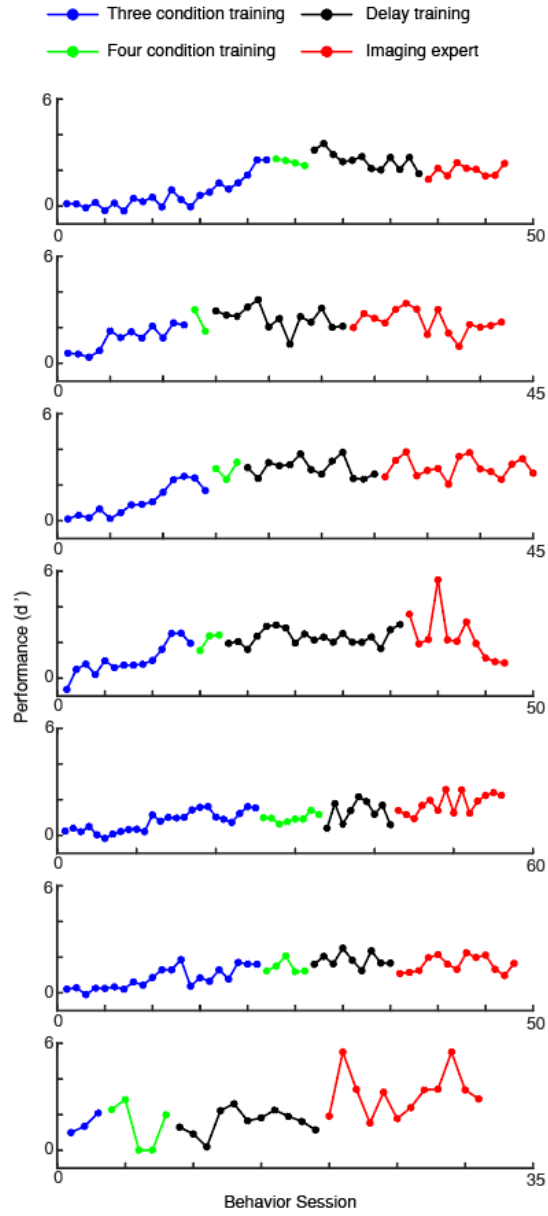
Fig. S6. DNMS task performance during training and imaging for individual animals.
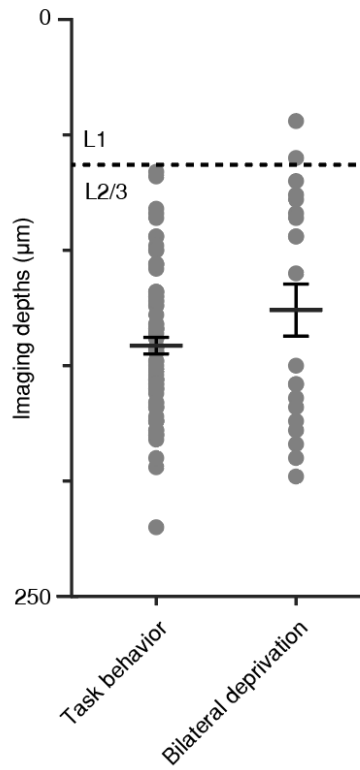
Fig. S7. Imaging depths for *in vivo* experiments. Imaging depths relative to the pial surface for task behavior and bilateral whisker deprivation experiments. Individual field of views (circles) along with mean±s.e.m. (lines) are shown.
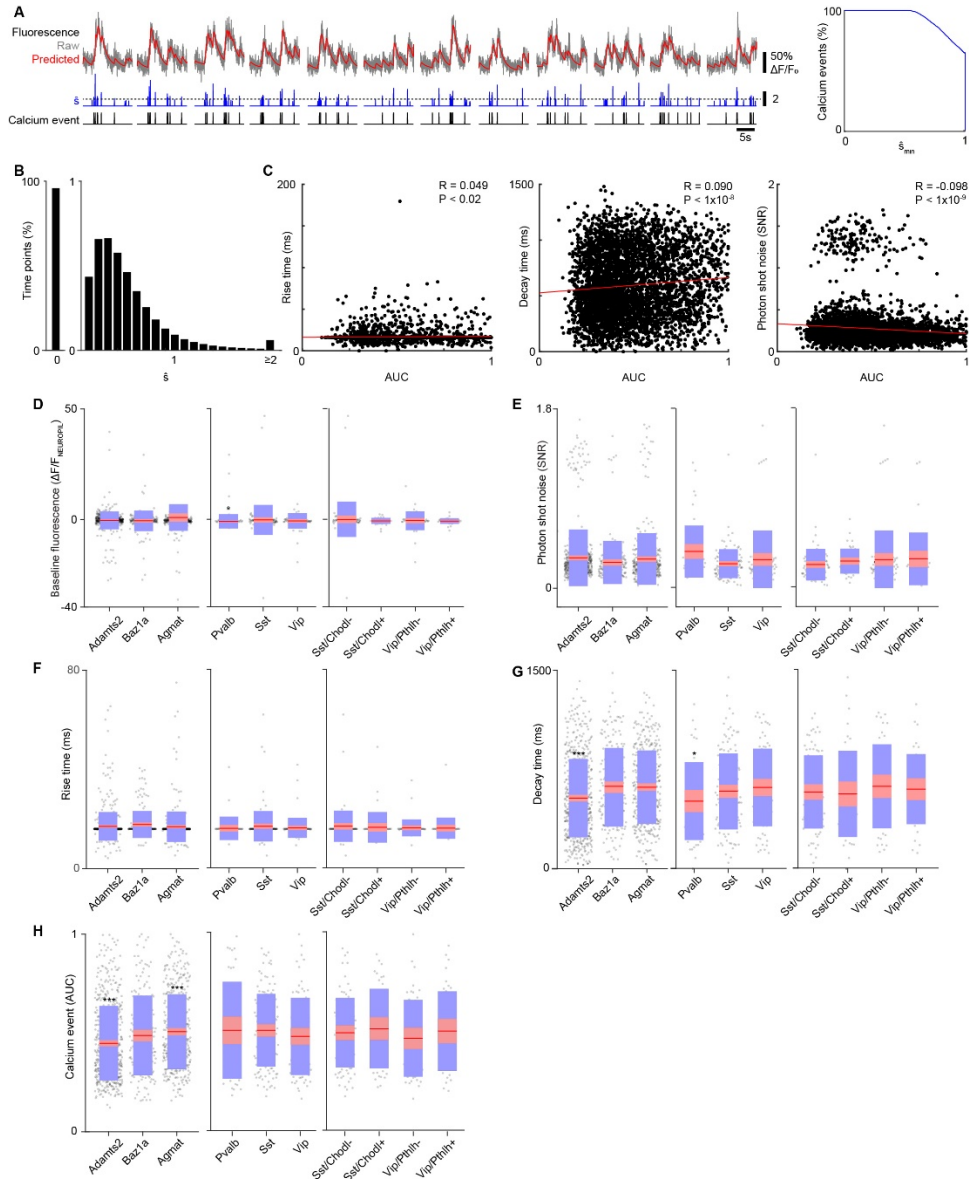
Fig. S8. Calcium kinetics and spike estimation across cell types. (**A**) Example of spike estimate from calcium signal using OASIS (left). Raw signals are fit using an auto-regressive model. The predicted trace is then deconvolved into a calcium event estimate ($\hat{s}$) which is thresholded into binary spikes (left). Receiver operator characteristic (ROC) showing relationship between model performance across varying $\hat{s}$ threshold (right). (**B**) Distribution of deconvolved signals across cells prior to thresholding. (**C**) Scatter plot showing relationship between spike estimation performance from ROC analysis vs. modeled calcium rise time (left), modeled decay time (middle), and photon shot noise (right) across individual neurons (Pearson's correlation). (**D**) Baseline fluorescence intensity across cell types. (**E**) Photon shot noise across cell types. (**F**) Modeled rise times across cell types. (**G**) Modeled decay times across cell types. (**H**) Spike estimation performance across cell types. For (C-F), red line: mean; pink region: 95% confidence interval; blue region: s.d. (* $P < 0.05$; *** $P < 1\times10^{-5}$; two-tailed Student's *t*-test with Bonferroni-Holm post-hoc correction).
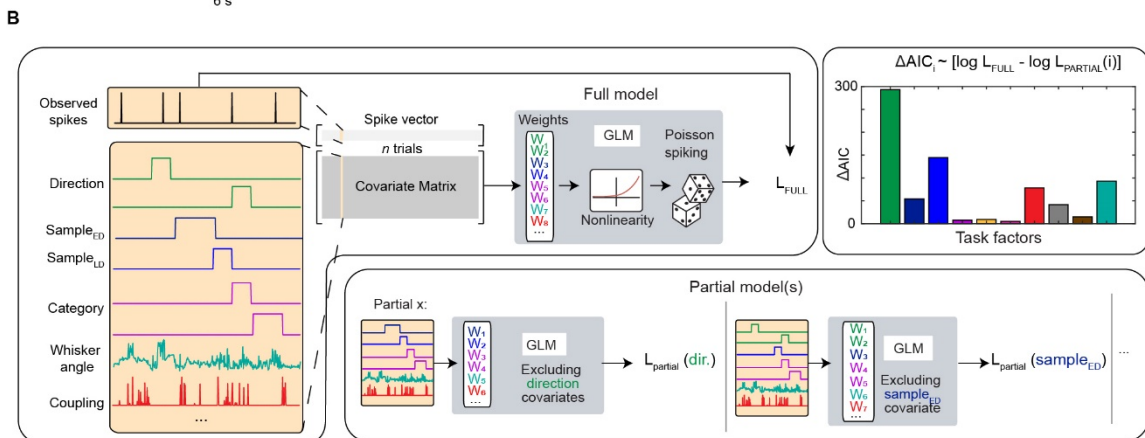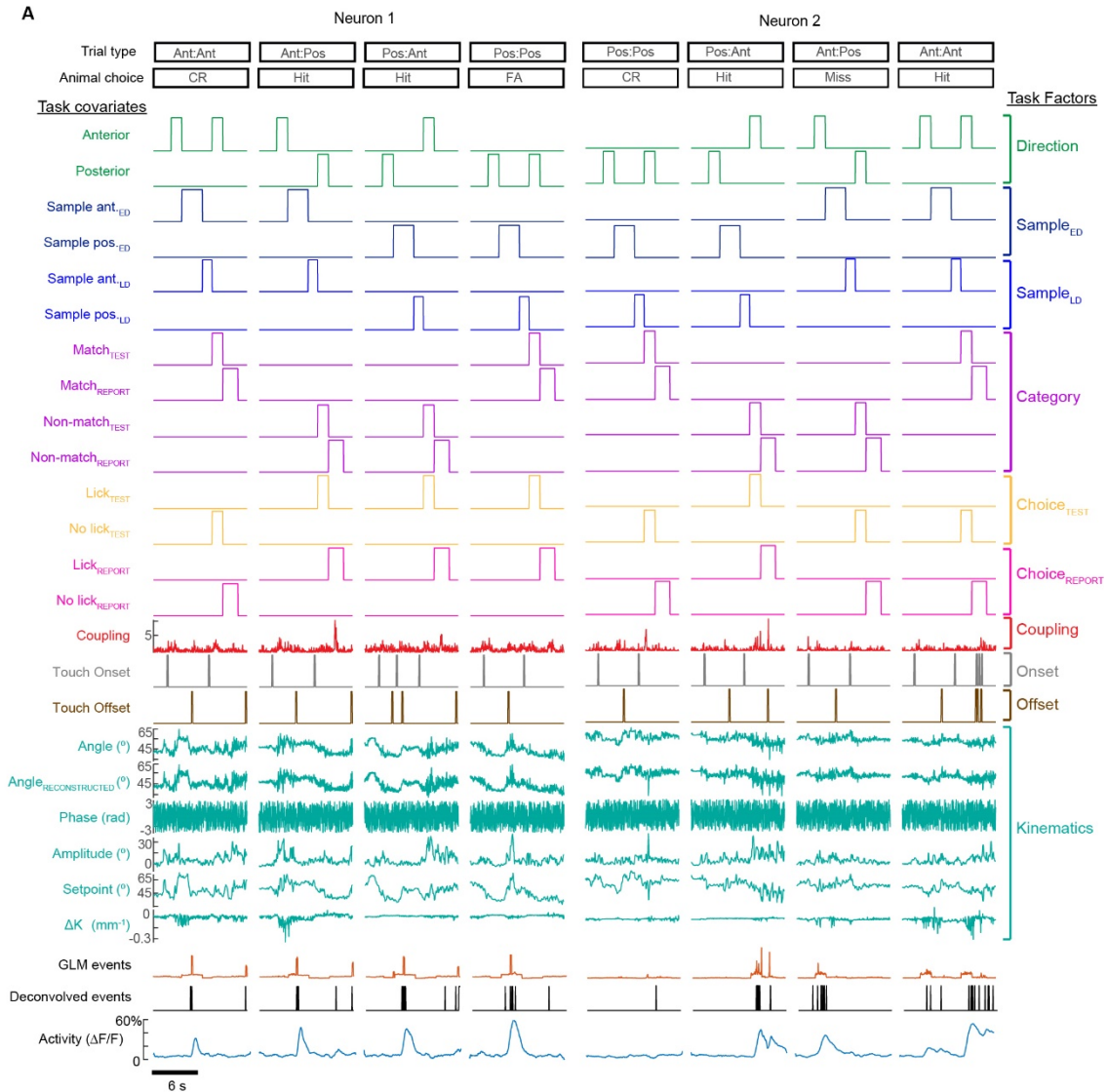
Fig. S9. Task encoding generalized linear model. (A) Overview of covariate representations and their corresponding task factors used in in the task-related GLM for two example neurons over four trials. **(B)** Schematic of full and partial models used to calculate ΔAIC for individual task factors.
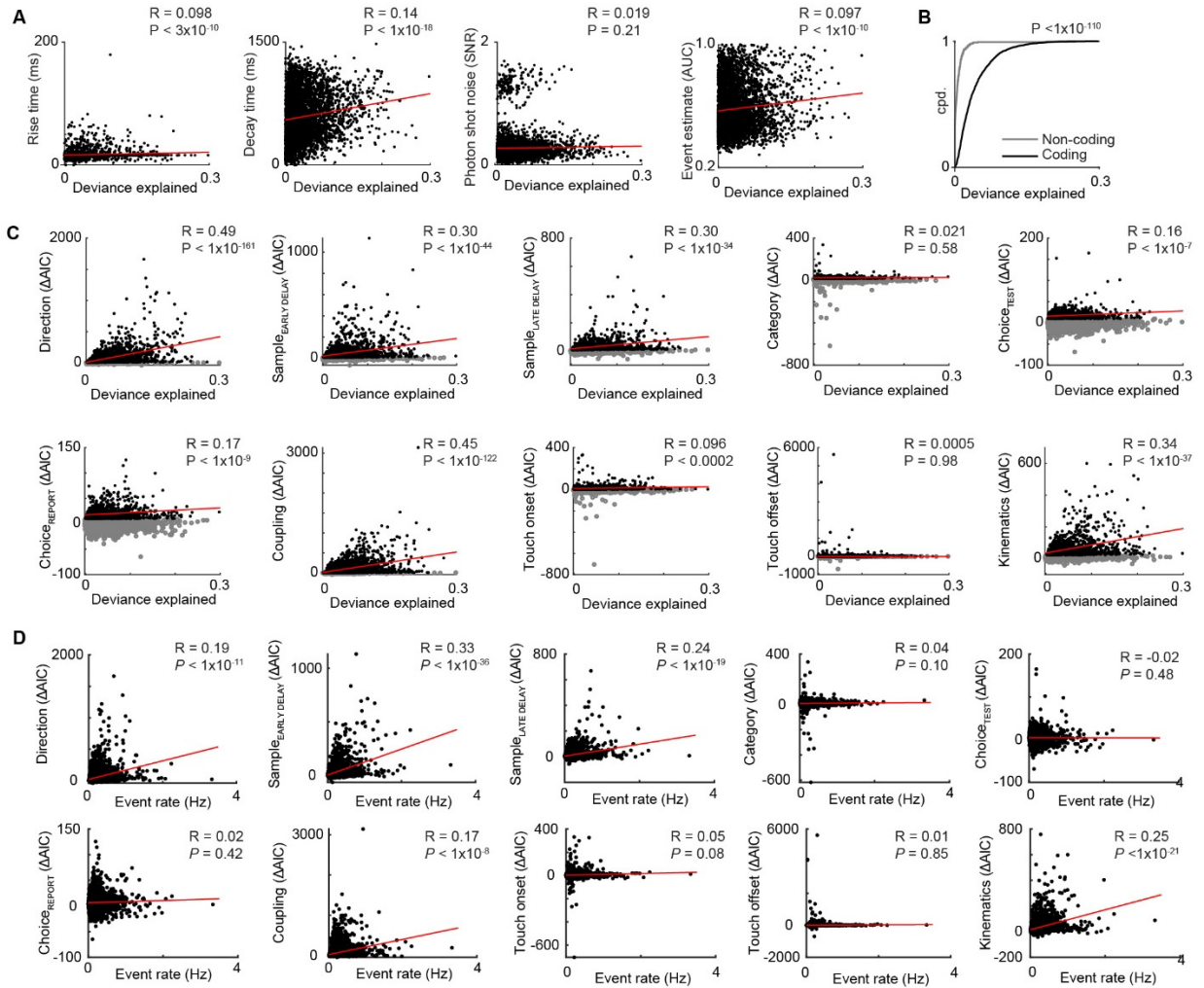
Fig. S10. Analysis of GLM model performance. (**A**) Relationship between calcium event detection obtained from OASIS vs. full model GLM fit for modeled rise time, modeled decay time, photon shot noise, and calcium event detection performance across individual cells (Pearson's correlation). (**B**) Comparison of model fit between non-coding neurons and those that encode at least one task factor (KS test). (**C**) Relationship between encoding strength of task factors vs. full model GLM fit across individual cells (Pearson's correlation). Significant ($P < 0.01$; black) and non-significant (grey) ΔAIC are shown determined by χ^2 test. (**D**) Relationship between encoding strength of task factors vs. calcium event rate across individual cells (Pearson's correlation).
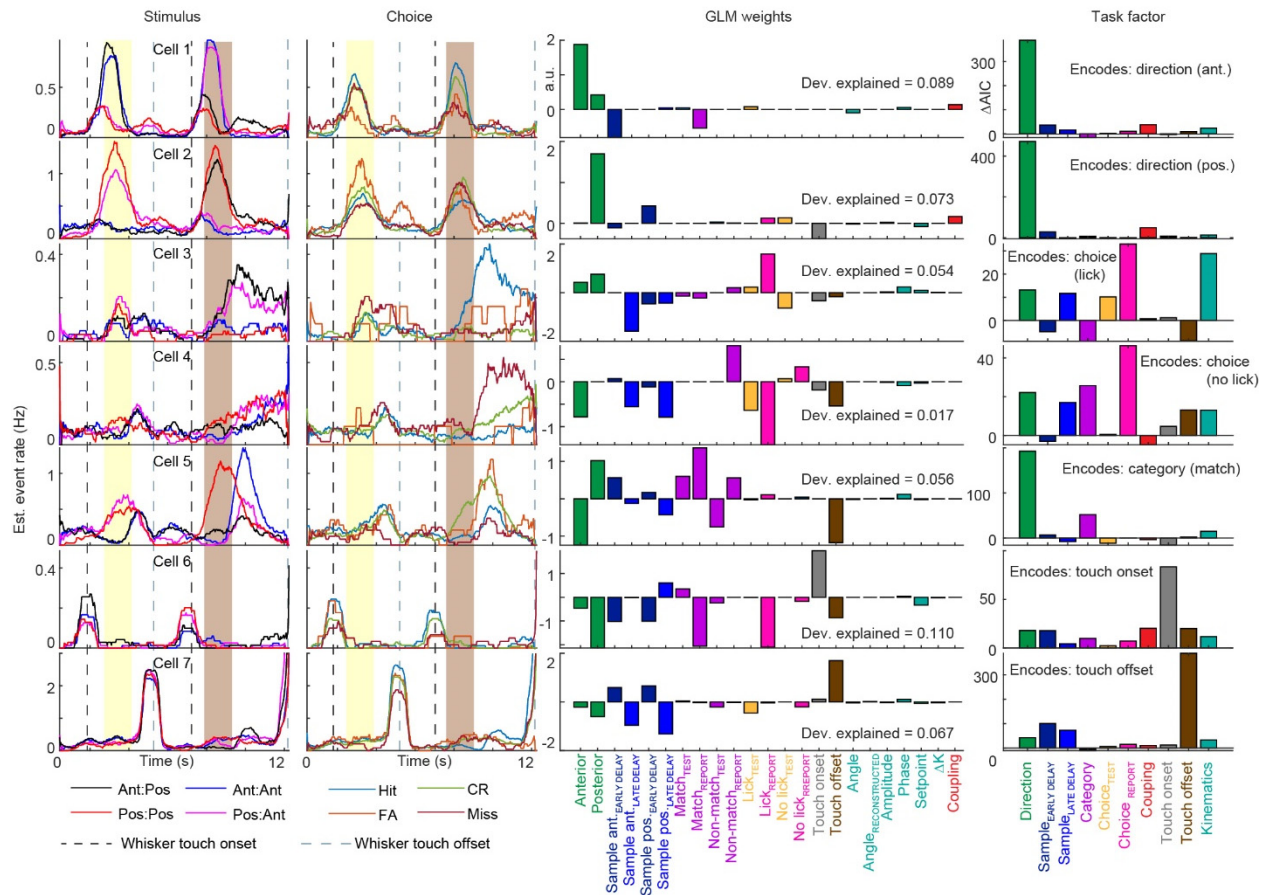
Fig. S11. Examples of task encoding neurons. For seven example neurons, average event rates are shown for stimulus conditions (far left) and animal's decision (middle left). Whisker touch onset and offset are also shown. Full model GLM weights for each covariate and deviance explained are shown (middle right). Encoding strength for each task factor are shown (far right).
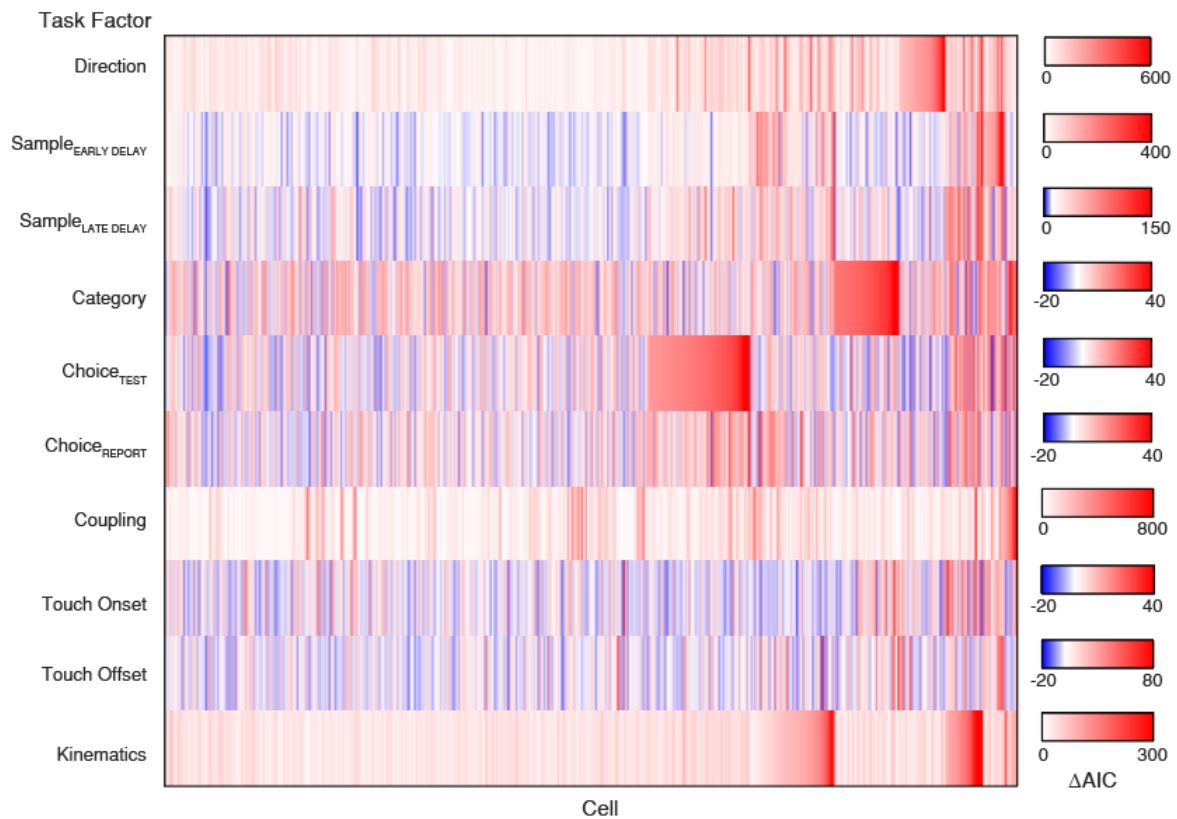
Fig. S12. Task encoding across neurons with identified cell types. For each neuron, encoding strength (ΔAIC) values for all task factors are shown. Neurons often exhibit "mixed selectivity" for multiple task factor. For visualization, ΔAIC ranges are scaled between the 1st and 99th percentile for each task factor. Cells are clustered and sorted using a Gaussian Mixture Model. *n* = 4,152 neurons from 7 animals.
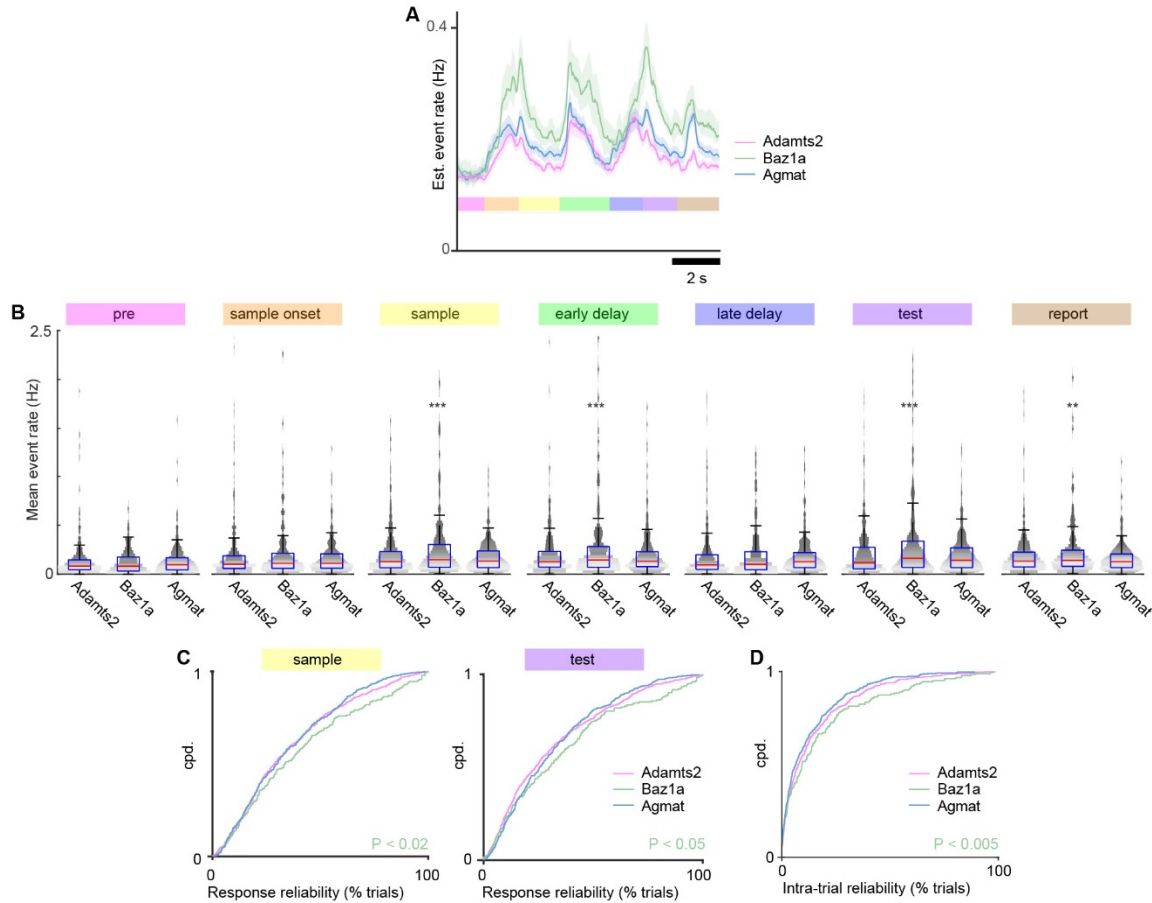
Fig. S13. Activity levels and response reliability of excitatory cell types. (**A**) Mean event rate for each excitatory cell type across the trial period. Shaded regions correspond to s.e.m. (**B**) Distribution of estimated event rate responses binned across each time period for neurons belonging to the three excitatory types. Whisker box plots are overlaid over violin plots to show distribution. (** $P < 0.01$, *** $P < 0.001$, right-tailed Student's t-test with Bonferroni-Holm post-hoc correction). Box centerline indicates median, box limits indicate upper and lower quartiles, and whiskers indicate 1.5x interquartile range. (**C,D**) Cumulative probability function of response reliability during the sample (left) and test (right) period (C) and intra-trial response reliability across the sample and test period (D) for the three excitatory types. Baz1a cells exhibit both greater response reliability and intra-trial reliability compared to other excitatory neurons (right-tailed Student's t-test with Bonferroni-Holm post-hoc correction). $n = 1,107$ neurons from 7 animals.
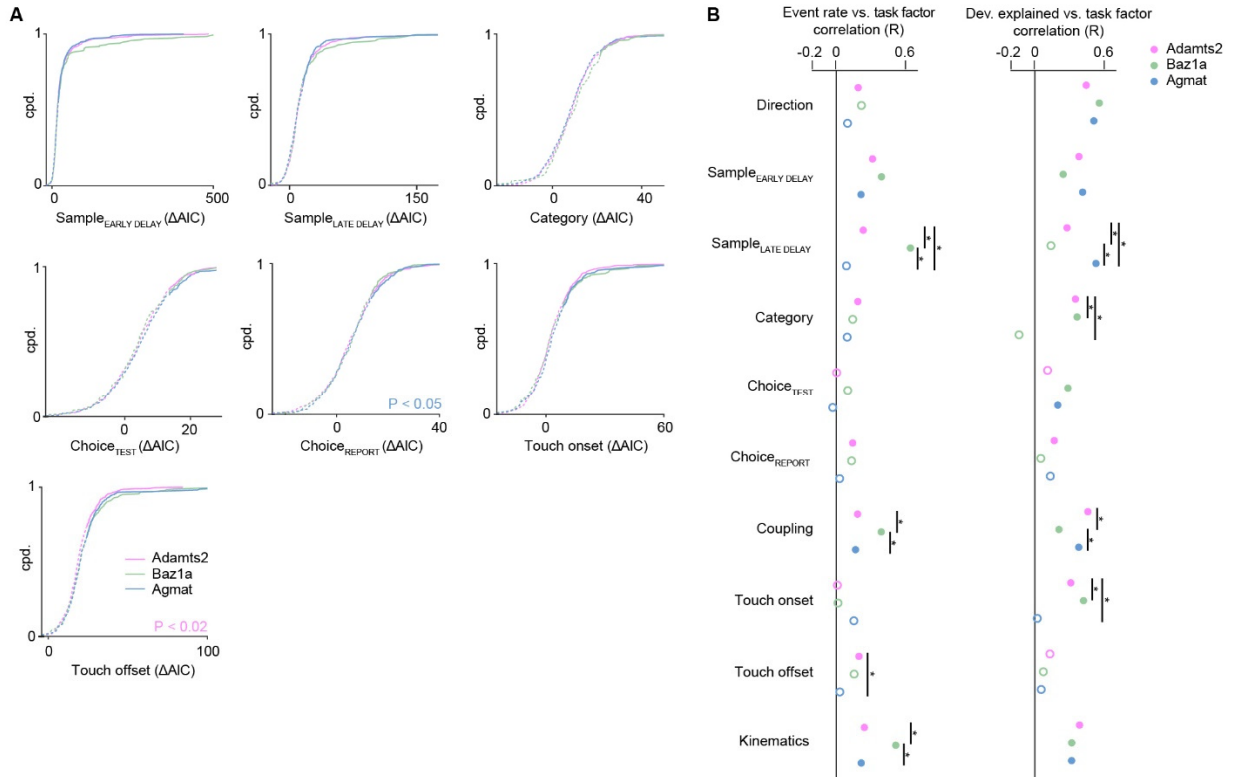
Fig. S14. Additional task encoding across L2/3 excitatory cell types. (**A**) Encoding strength to remaining task factors shown in Fig. 2 across excitatory cell types (Mann Whitney U Test). Solid and dotted lines correspond to significant ($P < 0.01$) and non-significant encoding strengths determined via χ^2 test. $n = 1,107$ neurons from 7 animals. (**B**) Relationship between encoding strength of task factors vs. calcium event rate (left) and task factors vs. full model GLM fit (right) across excitatory cell types. Significant ($P < 0.05$; filled circle) and non-significant (open circle) are shown (Pearson's correlation). Significant differences in correlations between cell types are also shown (*$P < 0.05$; correlation test, Bonferroni-Holm post-hoc correction).
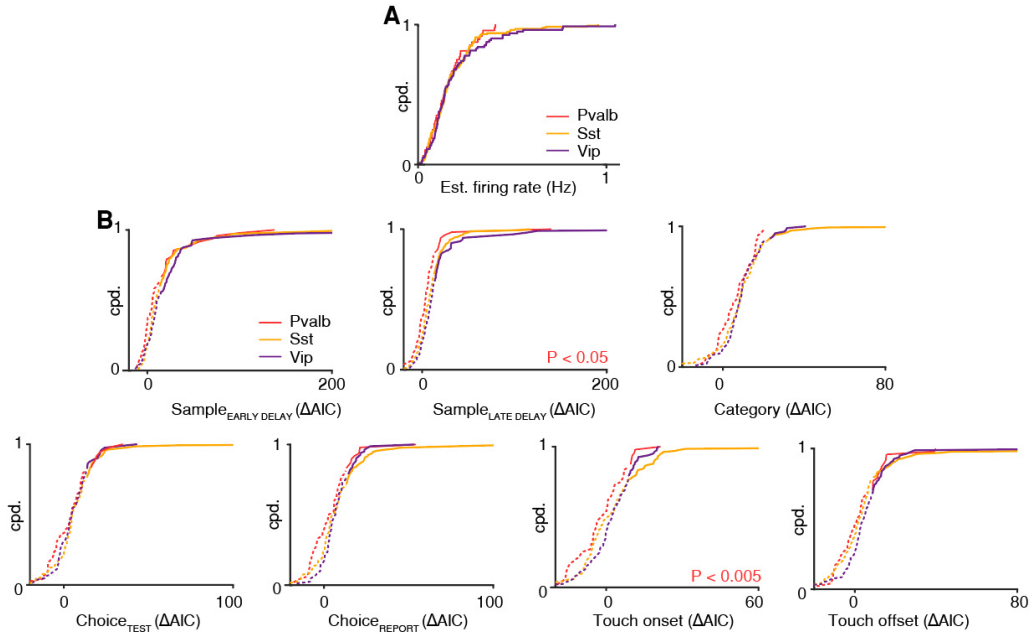
Fig. S15. Additional task encoding across inhibitory subclasses. (**A**) Cumulative probability distributions of estimated event rate across three inhibitory subclasses. (**B**) Encoding strength to remaining task factors not shown in Fig. 4 across inhibitory subclasses (Mann Whitney U test). Solid and dotted lines correspond to significant ($P < 0.01$) and non-significant encoding strengths determined via χ^2 test. $n = 272$ neurons from 7 animals.
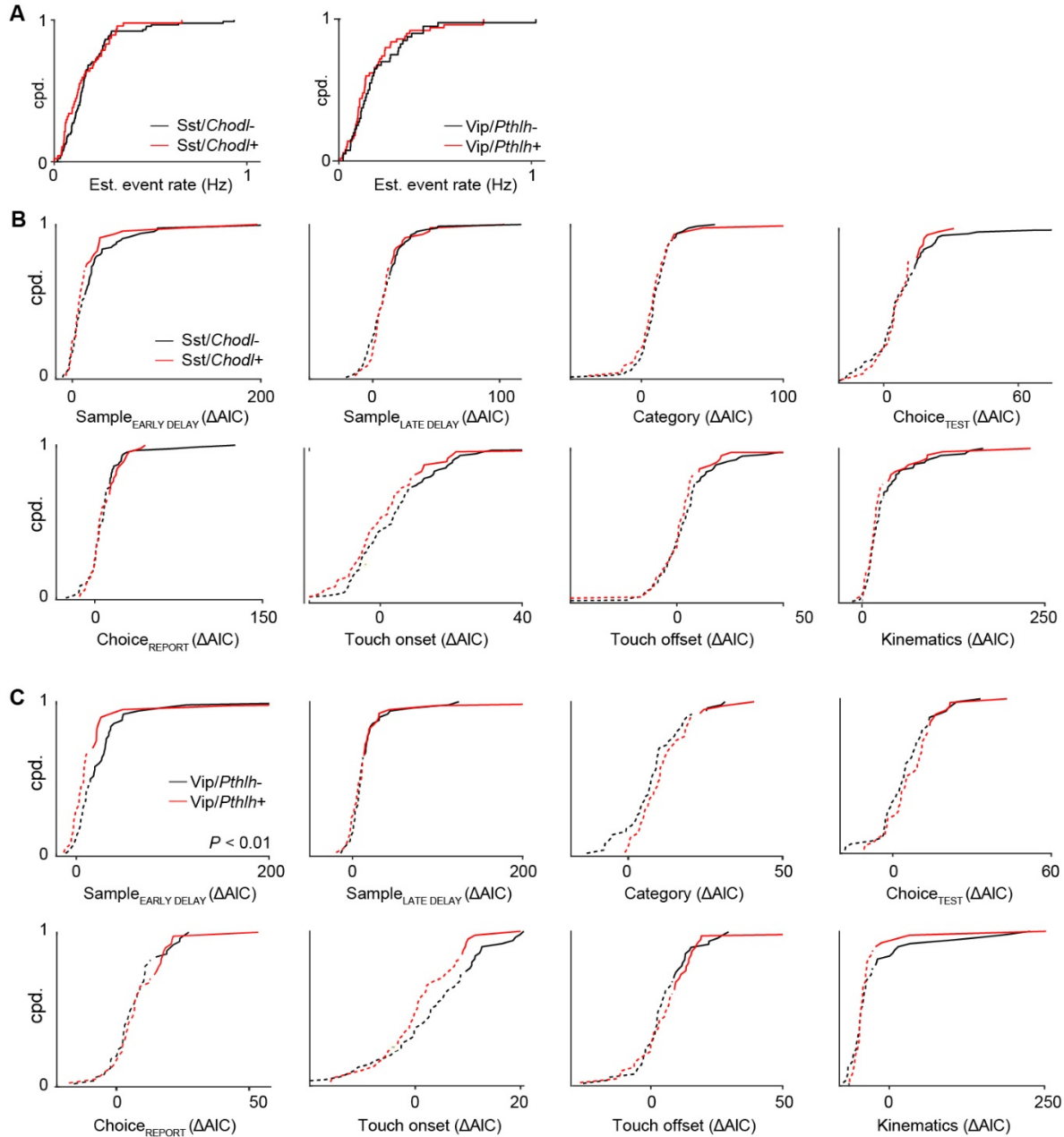
Fig. S16. Additional task encoding across inhibitory subclasses. (**A**) Cumulative probability distributions of estimated event rate across inhibitory subclasses. (**B**) Encoding strength to remaining task factors not shown in Fig. 4 across Sst subclasses. (**C**) Encoding strength to remaining task factors not shown in Fig. 4 across Vip subclasses (Mann Whitney U test). In (B-C)**,** solid and dotted lines correspond to significant ($P < 0.01$) and non-significant encoding strengths, determined via χ^2 test. $n = 224$ neurons from 7 animals.
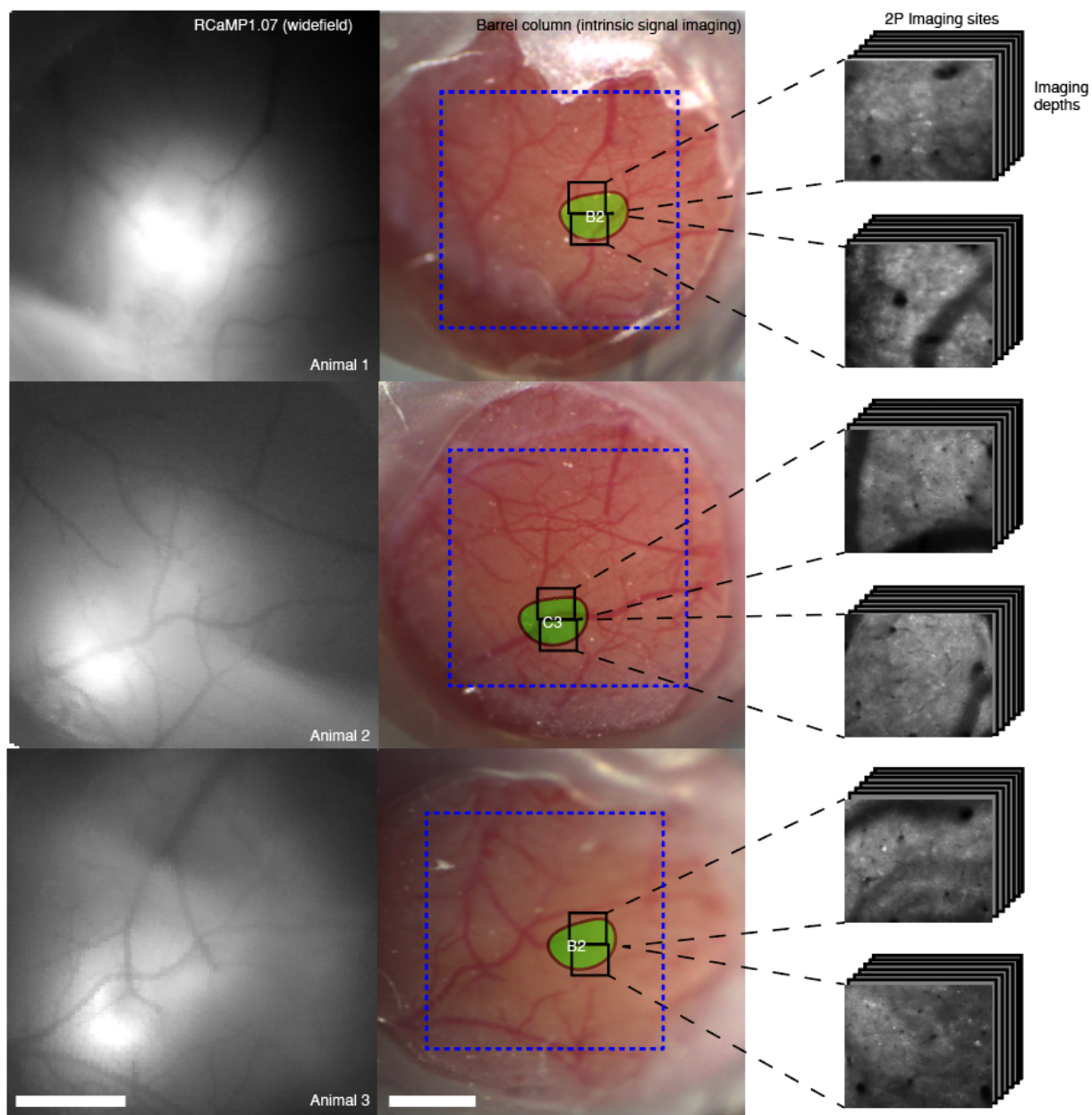
Fig. S17. *In vivo* **imaging site selection for bilateral deprivation experiments.** S1 barrel column selected for two-photon calcium imaging and whisker stimulation was selected based on RCaMP1.07 expression and intrinsic signal imaging. In the middle panel, a functionally mapped barrel column (green) is overlaid over a blood vessel map. Dotted blue outline indicates region of interest corresponding to widefield epi-fluorescent images of RCaMP1.07 expression (left panel). For each animal, two adjacent areas within selected barrel column were targeted (right). For each imaging session, eight field of views at different laminar depths were monitored. Scale bar: 1 mm.
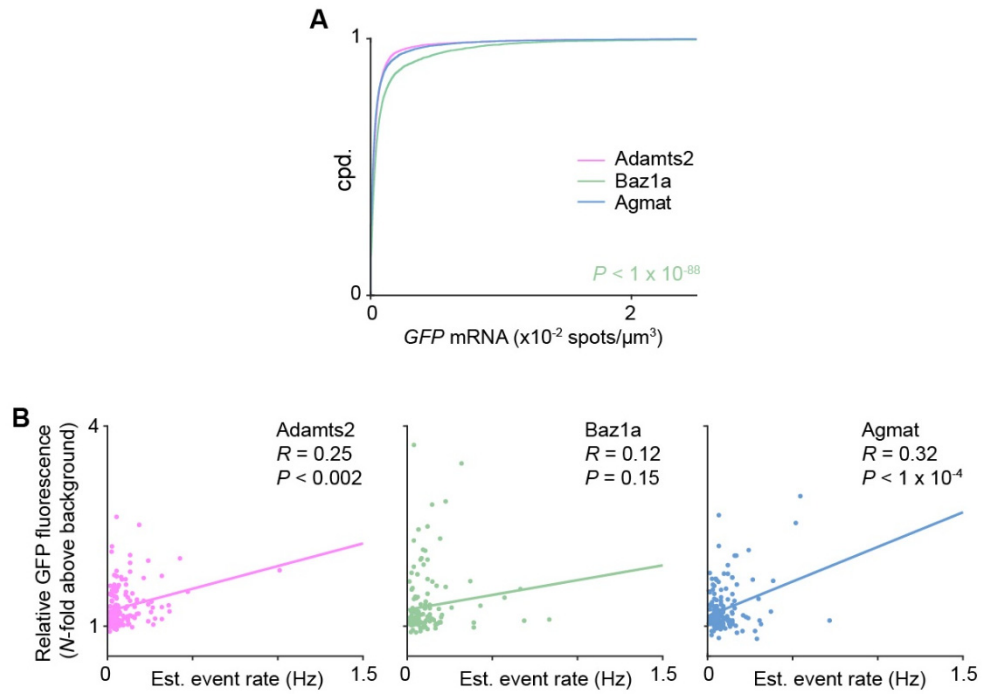
**Fig. S18. FosGFP expression across excitatory cell types.** (**A**) Cumulative probability distribution of *GFP* mRNA density from HCR-FISH in FosGFP mice across L2/3 excitatory cell types (Mann Whitney *U* test). $n = 26{,}396$ cells from 3 animals. (**B**) FosGFP fluorescence versus event rate across excitatory cell types (Pearson's correlation). $n = 181$ Adamts2, 136 Baz1a, and 153 Agmat cells from 3 animals.
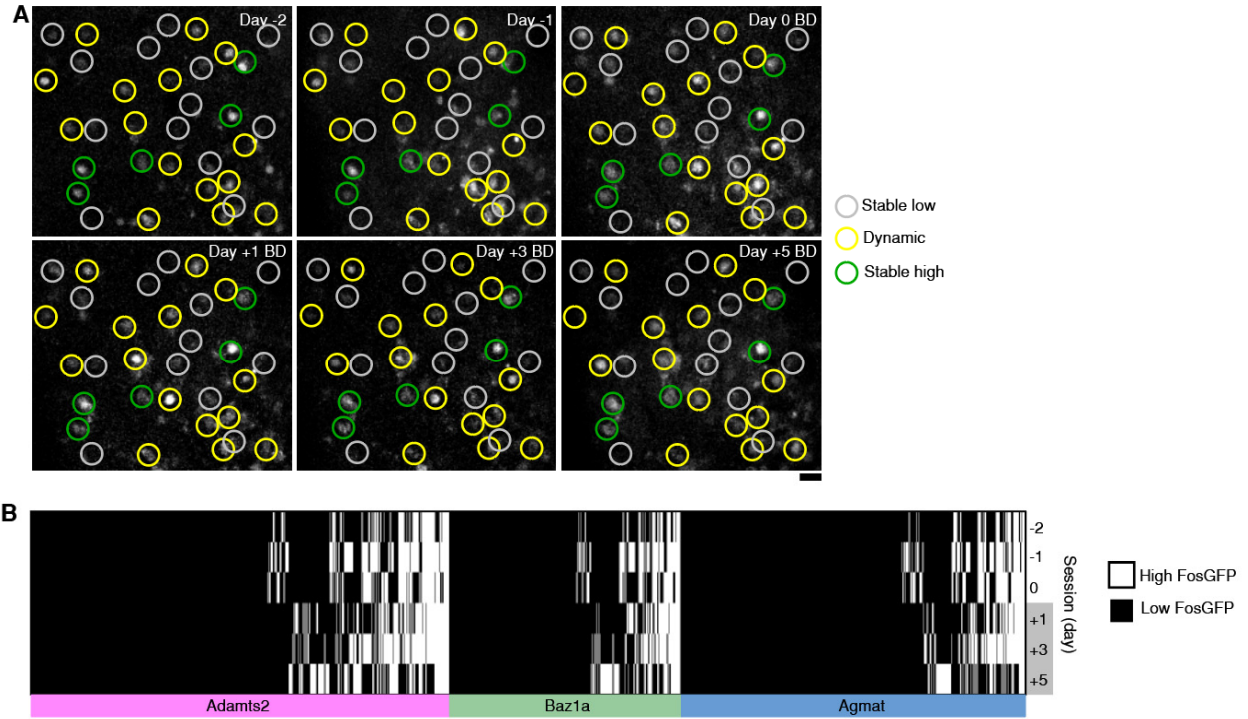
Fig. S19. Tracking experience-dependent FosGFP dynamics. (**A**) Chronic *in vivo* imaging of an example field of view before and during bilateral whisker deprivation. Stable low, dynamic, and stable high fosGFP cells are labeled. Scale bar: 30 µm. (**B**) FosGFP dynamics across excitatory cell types. *n* = 181 Adamts2, 136 Baz1a, and 153 Agmat cells from 3 animals.
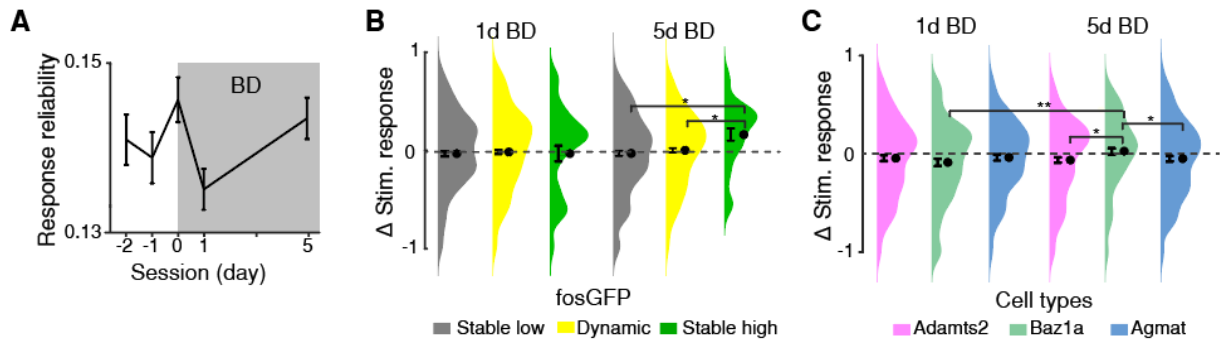
Fig. S20. Changes in stimulus response reliability during bilateral deprivation. (**A**) Mean trial-by-trial stimulus response reliability before and after BD across functionally imaged neurons. (**B**) Change in response reliability before BD versus at 1 day or 5 days BD across neurons with stable low, dynamic, and stable high fosGFP expression (two-tailed Student's t-test, $n = 790$ cells from 3 animals). (**C**) Change in response reliability before BD versus at 1 day or 5 days BD across excitatory cell types (χ^2 test, $n = 181$ Adamts2, 136 Baz1a, and 153 Agmat cells from 3 animals). Error bars = s.e.m. (* $P < 0.05$, ** $P < 0.01$).
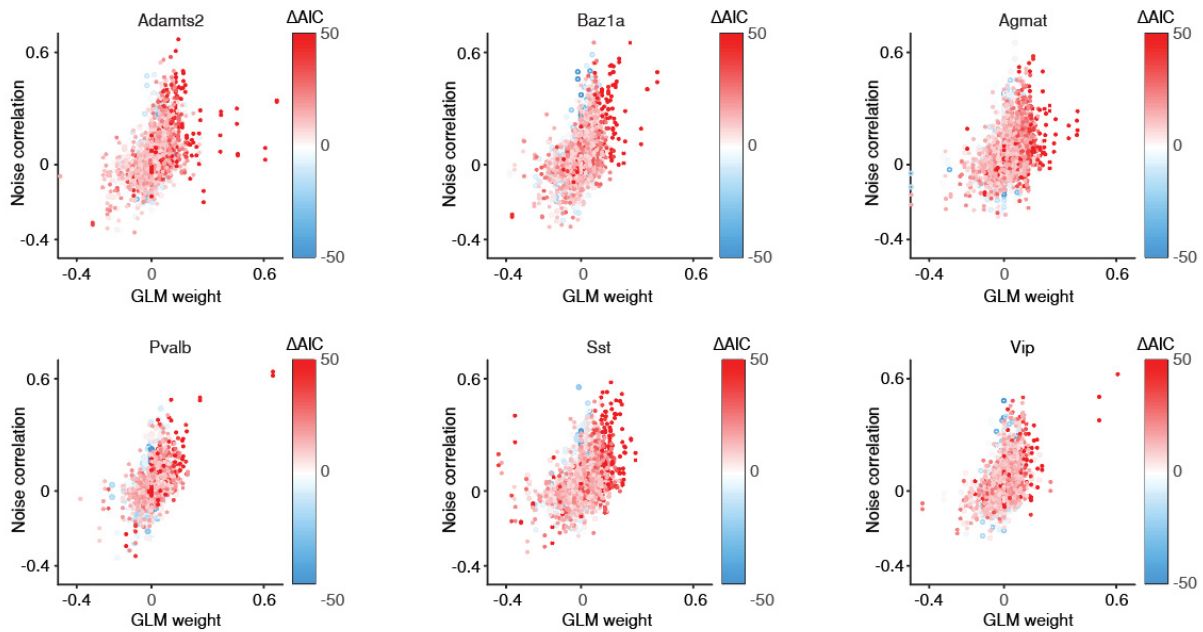
Fig. S21. Analysis of cell type coupling factors. For each cell type coupling factor, the relationship between an independently calculated noise correlation and the covariate weight to the cell type population activity from the GLM is shown for each neuron. The encoding strength for each coupling cell type factor is shown in color. Significant encoding strengths ($P < 0.01$; filled circle) and non-significant encoding strengths (open circle) are also shown, determined via χ^2 test.
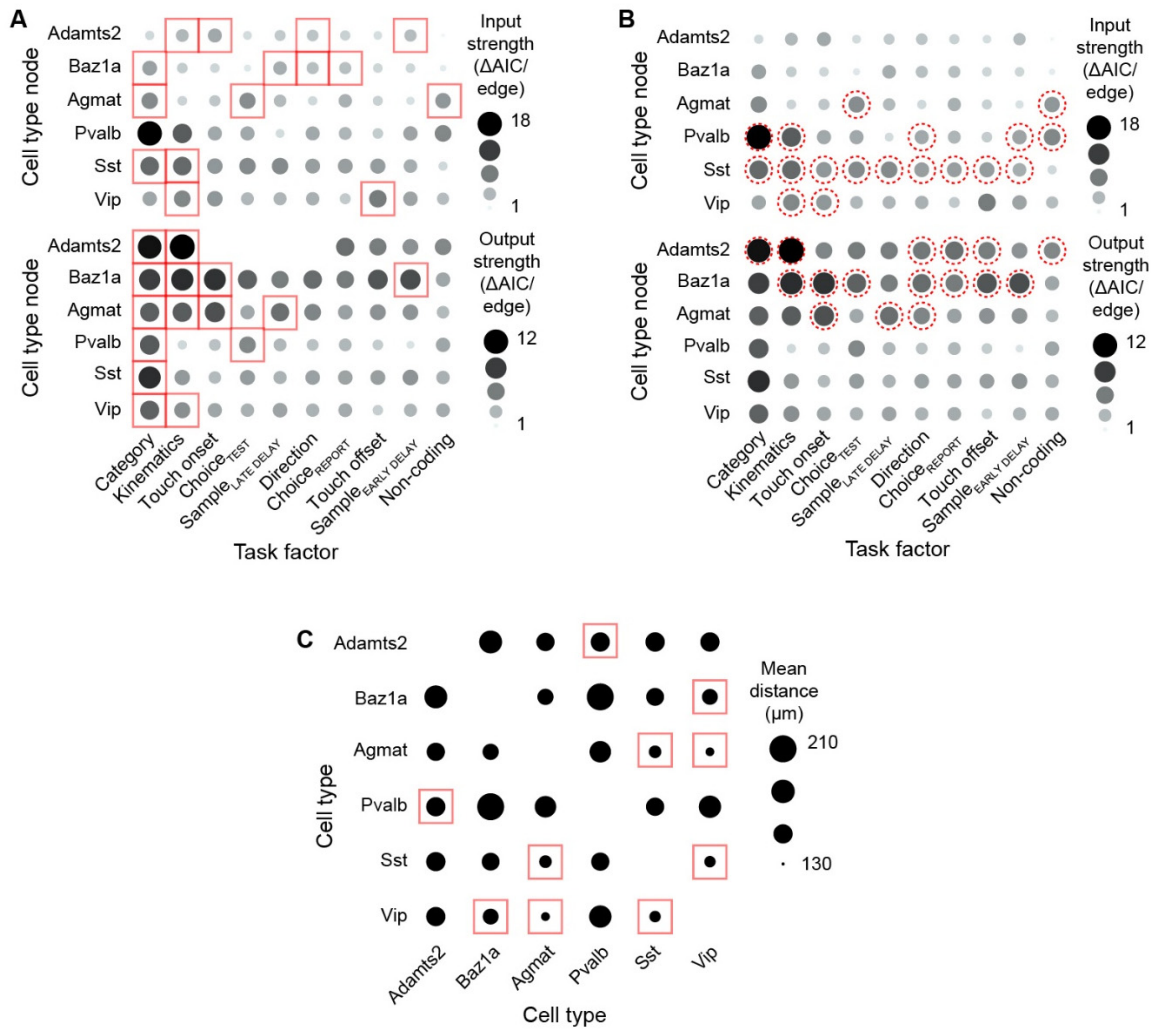
Fig. S22. Comparison of network node strengths and spatial clustering of cell types. (**A**) Input (top) and output (bottom) node strength for different cell types were compared across task networks. Significantly higher node strengths are noted with red box ($P < 0.05$, bootstrap test). (**B**) Input and output node strength for different cell types were compared within each task network. Significantly higher node strengths are noted with red dotted circle ($P < 0.05$, bootstrap test). (**C**) Mean distance between neuron pairs of identified cell types from *in vivo* imaging experiments. Cell type pairs showing significant clustering are noted with red box ($P < 0.05$, bootstrap test).

References and Notes

1. B. Tasic, Z. Yao, L. T. Graybuck, K. A. Smith, T. N. Nguyen, D. Bertagnolli, J. Goldy, E. Garren, M. N. Economo, S. Viswanathan, O. Penn, T. Bakken, V. Menon, J. Miller, O. Fong, K. E. Hirokawa, K. Lathia, C. Rimorin, M. Tieu, R. Larsen, T. Casper, E. Barkan, M. Kroll, S. Parry, N. V. Shapovalova, D. Hirschstein, J. Pendergraft, H. A. Sullivan, T. K. Kim, A. Szafer, N. Dee, P. Groblewski, I. Wickersham, A. Cetin, J. A. Harris, B. P. Levi, S. M. Sunkin, L. Madisen, T. L. Daigle, L. Looger, A. Bernard, J. Phillips, E. Lein, M. Hawrylycz, K. Svoboda, A. R. Jones, C. Koch, H. Zeng, Shared and distinct transcriptomic cell types across neocortical areas. *Nature* **563**, 72–78 (2018).

2. A. Zeisel, H. Hochgerner, P. Lönnerberg, A. Johnsson, F. Memic, J. van der Zwan, M. Häring, E. Braun, L. E. Borm, G. La Manno, S. Codeluppi, A. Furlan, K. Lee, N. Skene, K. D. Harris, J. Hjerling-Leffler, E. Arenas, P. Ernfors, U. Marklund, S. Linnarsson, Molecular architecture of the mouse nervous system. *Cell* **174**, 999–1014.e22 (2018).

3. E. Klingler, A. De la Rossa, S. Fièvre, K. Devaraju, P. Abe, D. Jabaudon, A translaminar genetic logic for the circuit identity of intracortically projecting neurons. *Curr. Biol.* **29**, 332–339.e5 (2019).

4. L. C. Greig, M. B. Woodworth, M. J. Galazo, H. Padmanabhan, J. D. Macklis, Molecular logic of neocortical projection neuron specification, development and diversity. *Nat. Rev. Neurosci.* **14**, 755–769 (2013).

5. L. Lim, D. Mi, A. Llorca, O. Marín, Development and functional diversification of cortical interneurons. *Neuron* **100**, 294–313 (2018).

6. S. A. Sorensen, A. Bernard, V. Menon, J. J. Royall, K. J. Glattfelder, T. Desta, K. Hirokawa, M. Mortrud, J. A. Miller, H. Zeng, J. G. Hohmann, A. R. Jones, E. S. Lein, Correlated gene expression and target specificity demonstrate excitatory projection neuron diversity. *Cereb. Cortex* **25**, 433–449 (2015).

7. A. Paul, M. Crow, R. Raudales, M. He, J. Gillis, Z. J. Huang, Transcriptional architecture of synaptic communication delineates GABAergic neuron identity. *Cell* **171**, 522–539.e20 (2017).

8. A. Kepecs, G. Fishell, Interneuron cell types are fit to function. *Nature* **505**, 318–326 (2014).

9. K. D. Harris, G. M. Shepherd, The neocortical circuit: Themes and variations. *Nat. Neurosci.* **18**, 170–181 (2015).

10. T. L. Daigle, L. Madisen, T. A. Hage, M. T. Valley, U. Knoblich, R. S. Larsen, M. M. Takeno, L. Huang, H. Gu, R. Larsen, M. Mills, A. Bosma-Moody, L. A. Siverts, M. Walker, L. T. Graybuck, Z. Yao, O. Fong, T. N. Nguyen, E. Garren, G. H. Lenz, M. Chavarha, J. Pendergraft, J. Harrington, K. E. Hirokawa, J. A. Harris, P. R. Nicovich, M. J. McGraw, D. R. Ollerenshaw, K. A. Smith, C. A. Baker, J. T. Ting, S. M. Sunkin, J. Lecoq, M. Z. Lin, E. S. Boyden, G. J. Murphy, N. M. da Costa, J. Waters, L. Li, B. Tasic, H. Zeng, A suite of transgenic driver and reporter mouse lines with enhanced brain-cell-type targeting and functionality. *Cell* **174**, 465–480.e22 (2018).

11. A. G. Khan, J. Poort, A. Chadwick, A. Blot, M. Sahani, T. D. Mrsic-Flogel, S. B. Hofer, Distinct learning-induced changes in stimulus selectivity and interactions of GABAergic interneuron classes in visual cortex. *Nat. Neurosci.* **21**, 851–859 (2018).

12. K. H. Chen, A. N. Boettiger, J. R. Moffitt, S. Wang, X. Zhuang, RNA imaging. Spatially resolved, highly multiplexed RNA profiling in single cells. *Science* **348**, aaa6090 (2015).

13. H. M. T. Choi, M. Schwarzkopf, M. E. Fornace, A. Acharya, G. Artavanis, J. Stegmaier, A. Cunha, N. A. Pierce, Third-generation in situ hybridization chain reaction: Multiplexed, quantitative, sensitive, versatile, robust. *Development* **145**, dev165753 (2018).

14. S. Shah, E. Lubeck, M. Schwarzkopf, T. F. He, A. Greenbaum, C. H. Sohn, A. Lignell, H. M. T. Choi, V. Gradinaru, N. A. Pierce, L. Cai, Single-molecule RNA detection at depth by hybridization chain reaction and tissue hydrogel embedding and clearing. *Development* **143**, 2862–2867 (2016).

15. E. Lubeck, A. F. Coskun, T. Zhiyentayev, M. Ahmad, L. Cai, Single-cell in situ RNA profiling by sequential hybridization. *Nat. Methods* **11**, 360–361 (2014).

16. X. Wang, W. E. Allen, M. A. Wright, E. L. Sylwestrak, N. Samusik, S. Vesuna, K. Evans, C. Liu, C. Ramakrishnan, J. Liu, G. P. Nolan, F.-A. Bava, K. Deisseroth, Three-dimensional intact-tissue sequencing of single-cell transcriptional states. *Science* **361**, eaat5691 (2018).

17. P. R. Nicovich, M. J. Taormina, C. A. Baker, T. N. Nguyen, E. R. Thomsen, E. Garren, B. Long, M. Gorham, J. A. Miller, T. Hage, A. Bosma-Moody, G. J. Murphy, B. P. Levi, J. L. Close, B. Tasic, E. S. Lein, H. Zeng, Multimodal cell type correspondence by intersectional mFISH in intact tissues. bioRxiv [Preprint] 525451 (2019). doi:10.1101/525451.

18. J. L. Chen, F. F. Voigt, M. Javadzadeh, R. Krueppel, F. Helmchen, Long-range population dynamics of anatomically defined neocortical networks. *eLife* **5**, e14679 (2016).

19. J. B. Treweek, K. Y. Chan, N. C. Flytzanis, B. Yang, B. E. Deverman, A. Greenbaum, A. Lignell, C. Xiao, L. Cai, M. S. Ladinsky, P. J. Bjorkman, C. C. Fowlkes, V. Gradinaru, Whole-body tissue stabilization and selective extractions via tissue-hydrogel hybrids for high-resolution intact circuit mapping and phenotyping. *Nat. Protoc.* **10**, 1860–1896 (2015).

20. M. Ohkura, T. Sasaki, C. Kobayashi, Y. Ikegaya, J. Nakai, An improved genetically encoded red fluorescent $Ca2^+$ indicator for detecting optically evoked action potentials. *PLOS ONE* **7**, e39933 (2012).

21. Z. Yao, C. T. J. van Velthoven, T. N. Nguyen, J. Goldy, A. E. Sedeno-Cortes, F. Baftizadeh, D. Bertagnolli, T. Casper, M. Chiang, K. Crichton, S. L. Ding, O. Fong, E. Garren, A. Glandon, N. W. Gouwens, J. Gray, L. T. Graybuck, M. J. Hawrylycz, D. Hirschstein, M. Kroll, K. Lathia, C. Lee, B. Levi, D. McMillen, S. Mok, T. Pham, Q. Ren, C. Rimorin, N. Shapovalova, J. Sulc, S. M. Sunkin, M. Tieu, A. Torkelson, H. Tung, K. Ward, N. Dee, K. A. Smith, B. Tasic, H. Zeng, A taxonomy of transcriptomic cell types across the isocortex and hippocampal formation. *Cell* **184**, 3222-3241.e26 (2021).

22. E. Abs, R. B. Poorthuis, D. Apelblat, K. Muhammad, M. B. Pardi, L. Enke, D. Kushinsky, D.-L. Pu, M. F. Eizinger, K.-K. Conzelmann, I. Spiegel, J. J. Letzkus, Learning-related plasticity in dendrite-targeting layer 1 interneurons. *Neuron* **100**, 684–699.e6 (2018).

23. J. Yu, H. Hu, A. Agmon, K. Svoboda, Recruitment of GABAergic interneurons in the barrel cortex during active tactile behavior. *Neuron* **104**, 412–427.e4 (2019).

24. C. Condylis, E. Lowet, J. Ni, K. Bistrong, T. Ouellette, N. Josephs, J. L. Chen, Context-dependent sensory processing across primary and secondary somatosensory cortex. *Neuron* **106**, 515–525.e5 (2020).

25. J. W. Pillow, J. Shlens, L. Paninski, A. Sher, A. M. Litke, E. J. Chichilnisky, E. P. Simoncelli, Spatio-temporal correlations and visual signalling in a complete neuronal population. *Nature* **454**, 995–999 (2008).

26. C. A. Runyan, E. Piasini, S. Panzeri, C. D. Harvey, Distinct timescales of population coding across cortex. *Nature* **548**, 92–96 (2017).

27. L. Yassin, B. L. Benedetti, J.-S. Jouhanneau, J. A. Wen, J. F. A. Poulet, A. L. Barth, An embedded subnetwork of highly active neurons in the neocortex. *Neuron* **68**, 1043–1050 (2010).

28. J.-S. Jouhanneau, L. Ferrarese, L. Estebanez, N. J. Audette, M. Brecht, A. L. Barth, J. F. A. Poulet, Cortical fosGFP expression reveals broad receptive field excitatory neurons targeted by POm. *Neuron* **84**, 1065–1078 (2014).

29. E. L. Yap, M. E. Greenberg, Activity-regulated transcription: Bridging the gap between neural activity and behavior. *Neuron* **100**, 330–348 (2018).

30. A. L. Barth, R. C. Gerkin, K. L. Dean, Alteration of neuronal firing properties after in vivo experience in a FosGFP transgenic mouse. *J. Neurosci.* **24**, 6466–6475 (2004).

31. D. J. Margolis, H. Lütcke, K. Schulz, F. Haiss, B. Weber, S. Kügler, M. T. Hasan, F. Helmchen, Reorganization of cortical population activity imaged throughout long-term sensory deprivation. *Nat. Neurosci.* **15**, 1539–1546 (2012).

32. M. A. Gainey, D. E. Feldman, Multiple shared mechanisms for homeostatic plasticity in rodent somatosensory and visual cortex. *Philos. Trans. R. Soc. London B Biol. Sci.* **372**, 20160157 (2017).

33. A. C. Kwan, Y. Dan, Dissection of cortical microcircuits by single-neuron stimulation in vivo. *Curr. Biol.* **22**, 1459–1467 (2012).

34. B. Tasic, V. Menon, T. N. Nguyen, T. K. Kim, T. Jarsky, Z. Yao, B. Levi, L. T. Gray, S. A. Sorensen, T. Dolbeare, D. Bertagnolli, J. Goldy, N. Shapovalova, S. Parry, C. Lee, K. Smith, A. Bernard, L. Madisen, S. M. Sunkin, M. Hawrylycz, C. Koch, H. Zeng, Adult mouse cortical cell taxonomy revealed by single cell transcriptomics. *Nat. Neurosci.* **19**, 335–346 (2016).

35. R. Tomioka, K. Okamoto, T. Furuta, F. Fujiyama, T. Iwasato, Y. Yanagawa, K. Obata, T. Kaneko, N. Tamamaki, Demonstration of long-range GABAergic connections distributed throughout the mouse neocortex. *Eur. J. Neurosci.* **21**, 1587–1600 (2005).

36. M. He, J. Tucciarone, S. Lee, M. J. Nigro, Y. Kim, J. M. Levine, S. M. Kelly, I. Krugikov, P. Wu, Y. Chen, L. Gong, Y. Hou, P. Osten, B. Rudy, Z. J. Huang, Strategies and Tools for Combinatorial Targeting of GABAergic Neurons in Mouse Cerebral Cortex. *Neuron* **91**, 1228–1243 (2016).

37. D. Gerashchenko, J. P. Wisor, D. Burns, R. K. Reh, P. J. Shiromani, T. Sakurai, H. O. de la Iglesia, T. S. Kilduff, Identification of a population of sleep-active cerebral cortex neurons. *Proc. Natl. Acad. Sci. U.S.A.* **105**, 10227–10232 (2008).

38. A. Dudai, N. Yayon, V. Lerner, G. I. Tasaka, Y. Deitcher, K. Gorfine, N. Niederhoffer, A. Mizrahi, H. Soreq, M. London, Barrel cortex VIP/ChAT interneurons suppress sensory responses in vivo. *PLOS Biol.* **18**, e3000613 (2020).

39. A. Prönneke, B. Scheuer, R. J. Wagener, M. Möck, M. Witte, J. F. Staiger, Characterizing VIP neurons in the barrel cortex of VIPcre/tdTomato mice reveals layer-specific differences. *Cereb. Cortex* **25**, 4854–4868 (2015).

40. S. Lee, I. Kruglikov, Z. J. Huang, G. Fishell, B. Rudy, A disinhibitory circuit mediates motor integration in the somatosensory cortex. *Nat. Neurosci.* **16**, 1662–1670 (2013).

41. H. Hioki, J. Sohn, H. Nakamura, S. Okamoto, J. Hwang, Y. Ishida, M. Takahashi, H. Kameda, Preferential inputs from cholecystokinin-positive neurons to the somatic compartment of parvalbumin-expressing neurons in the mouse primary somatosensory cortex. *Brain Res.* **1695**, 18–30 (2018).

42. H. Taniguchi, M. He, P. Wu, S. Kim, R. Paik, K. Sugino, D. Kvitsiani, Y. Fu, J. Lu, Y. Lin, G. Miyoshi, Y. Shima, G. Fishell, S. B. Nelson, Z. J. Huang, A resource of Cre driver lines for genetic targeting of GABAergic neurons in cerebral cortex. *Neuron* **71**, 995–1013 (2011).

43. T. R. Reardon, A. J. Murray, G. F. Turi, C. Wirblich, K. R. Croce, M. J. Schnell, T. M. Jessell, A. Losonczy, Rabies virus CVS-N2c(ΔG) strain enhances retrograde synaptic transfer and neuronal viability. *Neuron* **89**, 711–724 (2016).

44. M. E. Diamond, M. von Heimendahl, P. M. Knutsen, D. Kleinfeld, E. Ahissar, 'Where' and 'what' in the whisker sensorimotor system. *Nat. Rev. Neurosci.* **9**, 601–612 (2008).

45. N. L. Xu, M. T. Harnett, S. R. Williams, D. Huber, D. H. O'Connor, K. Svoboda, J. C. Magee, Nonlinear dendritic integration of sensory and motor input during an active sensing task. *Nature* **492**, 247–251 (2012).

46. G. Doron, J. N. Shin, N. Takahashi, M. Drüke, C. Bocklisch, S. Skenderi, L. de Mont, M. Toumazou, J. Ledderose, M. Brecht, R. Naud, M. E. Larkum, Perirhinal input to neocortical layer 1 controls learning. *Science* **370**, eaaz3136 (2020).

47. N. Spruston, Pyramidal neurons: Dendritic structure and synaptic integration. *Nat. Rev. Neurosci.* **9**, 206–221 (2008).

48. L. E. Williams, A. Holtmaat, Higher-order thalamocortical inputs gate synaptic long-term potentiation via disinhibition. *Neuron* **101**, 91–102.e4 (2019).

49. Y. Wang, M. Toledo-Rodriguez, A. Gupta, C. Wu, G. Silberberg, J. Luo, H. Markram, Anatomical, physiological and molecular properties of Martinotti cells in the somatosensory cortex of the juvenile rat. *J. Physiol.* **561**, 65–90 (2004).

50. S. Loebrich, E. Nedivi, The function of activity-regulated genes in the nervous system. *Physiol. Rev.* **89**, 1079–1103 (2009).

51. C. Condylis, A. Ghanbari, N. Manjrekar, K. Bistrong, S. Yao, Z. Yao, T. N. Nguyen, H. Zeng, B. Tasic, J. Chen, Dense functional and molecular readout of a circuit hub in sensory cortex. G-Node (2021); doi:10.12751/g-node.7q0lz0.

52. N. G. Clack, D. H. O'Connor, D. Huber, L. Petreanu, A. Hires, S. Peron, K. Svoboda, E. W. Myers, Automated tracking of whiskers in videos of head fixed rodents. *PLOS Comput. Biol.* **8**, e1002591 (2012).

53. D. N. Hill, J. C. Curtis, J. D. Moore, D. Kleinfeld, Primary motor cortex reports efferent control of vibrissa motion on multiple timescales. *Neuron* **72**, 344–356 (2011).

54. E. A. Pnevmatikakis, D. Soudry, Y. Gao, T. A. Machado, J. Merel, D. Pfau, T. Reardon, Y. Mu, C. Lacefield, W. Yang, M. Ahrens, R. Bruno, T. M. Jessell, D. S. Peterka, R. Yuste, L. Paninski, Simultaneous denoising, deconvolution, and demixing of calcium imaging data. *Neuron* **89**, 285–299 (2016).

55. P. Rupprecht, S. Carta, A. Hoffmann, M. Echizen, K. Kitamura, F. Helmchen, R. W. Friedrich, A deep learning toolbox for noise-optimized, generalized spike inference from calcium imaging data. bioRxiv [Preprint] 272450 (2020). doi:10.1101/2020.08.31.272450.

56. H. M. T. Choi, M. Schwarzkopf, M. E. Fornace, A. Acharya, G. Artavanis, J. Stegmaier, A. Cunha, N. A. Pierce, Third-generation in situ hybridization chain reaction: Multiplexed, quantitative, sensitive, versatile, robust. *Development* **145**, dev165753 (2018).

57. A. Bria, G. Iannello, TeraStitcher—A tool for fast automatic 3D-stitching of teravoxel-sized microscopy images. *BMC Bioinformatics* **13**, 316 (2012).

58. M. Guizar-Sicairos, S. T. Thurman, J. R. Fienup, Efficient subpixel image registration algorithms. *Opt. Lett.* **33**, 156–158 (2008).

59. X. Lou, M. Kang, P. Xenopoulos, S. Muñoz-Descalzo, A. K. Hadjantonakis, A rapid and efficient 2D/3D nuclear segmentation method for analysis of early mouse embryo and stem cell image data. *Stem Cell Reports* **2**, 382–397 (2014).

60. I. Arganda-Carreras, V. Kaynig, C. Rueden, K. W. Eliceiri, J. Schindelin, A. Cardona, H. Sebastian Seung, Trainable Weka Segmentation: A machine learning tool for microscopy pixel classification. *Bioinformatics* **33**, 2424–2426 (2017).

61. K. E. G. Magnusson, thesis, KTH Royal Institute of Technology (2016).

62. S. Axelrod, M. Cai, A. Carr, J. Freeman, D. Ganguli, J. Kiggins, B. Long, T. Tung, K. Yamauchi, starfish: Scalable pipelines for image-based transcriptomics. *J. Open Source Softw.* **6**, 2440 (2021).

63. I. M. Park, M. L. Meister, A. C. Huk, J. W. Pillow, Encoding and decoding in parietal cortex during sensorimotor decision-making. *Nat. Neurosci.* **17**, 1395–1403 (2014).

64. K. Y. Chan, M. J. Jang, B. B. Yoo, A. Greenbaum, N. Ravi, W.-L. Wu, L. Sánchez-Guardado, C. Lois, S. K. Mazmanian, B. E. Deverman, V. Gradinaru, Engineered AAVs

for efficient noninvasive gene delivery to the central and peripheral nervous systems. *Nat. Neurosci.* **20**, 1172–1179 (2017).

65. J. L. Nathanson, Y. Yanagawa, K. Obata, E. M. Callaway, Preferential labeling of inhibitory and excitatory cortical neurons by endogenous tropism of adeno-associated virus and lentivirus vectors. *Neuroscience* **161**, 441–450 (2009).

66. R. Tremblay, S. Lee, B. Rudy, GABAergic interneurons in the neocortex: From cellular properties to circuits. *Neuron* **91**, 260–292 (2016).

67. J. Friedrich, P. Zhou, L. Paninski, Fast online deconvolution of calcium imaging data. *PLOS Comput. Biol.* **13**, e1005423 (2017).

68. Y. Aponte, J. Bischofberger, P. Jonas, Efficient Ca^{2+} buffering in fast-spiking basket cells of rat hippocampus. *J. Physiol.* **586**, 2061–2075 (2008).

69. M. Minderer, K. D. Brown, C. D. Harvey, The spatial structure of neural encoding in mouse posterior cortex during navigation. *Neuron* **102**, 232–248.e11 (2019).

70. M. R. Cohen, A. Kohn, Measuring and interpreting neuronal correlations. *Nat. Neurosci.* **14**, 811–819 (2011).